A numerical method to determine the displacement spectrum of micro-plates in viscous fluids

A. Gesing, D. Platz, U. Schmid

Institute of Sensor and Actuator Systems, TU Wien, Gußhausstraße 27-29, 1040 Vienna, Austria

ABSTRACT

In this paper, we present a semi-numerical method for determining the dynamics of micro-resonators with finite width immersed in incompressible viscous fluids. The micro-resonator is modeled using Kirchhoff plate theory, and the hydrodynamic force acting on the plate is determined from a boundary integral formulation of the Stokes equations. The resulting equation of motion is solved with a continuous/discontinuous finite element method in which an interior penalty term imposes C^1-continuity to the plate's deflection. Numerical investigations show the method to be convergent with an exponent of the convergence rate equals 2. Examples demonstrate that the proposed method overcomes the limitations of existing semi-analytic methods, only applicable to beam geometries, considering arbitrary plate modes in the structure's dynamics and their effects on the fluid flow. Different resonator geometries are investigated for which displacement spectrum, mode shapes, and quality factors are not determinable with existent semi-analytic methods. Moreover, we find excellent agreement between simulated and experimental data, which has not been achieved even with purely numerical methods. The present method will allow the understanding of high quality factors of wide micro-resonators in viscous fluids and facilitate new applications in liquid atomic force microscopy and gas sensing in ambient and low-pressure conditions.

© 2021 The Authors. Published by Elsevier Ltd. This is an open access article under the CC BY license (http://creativecommons.org/licenses/by/4.0/).

1. Introduction

Resonant microelectromechanical systems (MEMS), also known as micro-resonators, are a success story and span a wide range of applications, e.g., atomic force microscopy (AFM) [52,25,29], energy harvesting [12], bio-mimetic robotic propulsion [14,23,33], viscosity sensors [11,35,46], micro-pumps [66] and micro-fanning [7].

A standard building block of micro-resonators is a thin elastic structure [8,49]. Micro-resonators operate using the structure's resonance frequencies, which typically range from a couple of kilohertz to tens of megahertz [8]. When the micro-resonator is in contact with a fluid, the fluid reduces the elastic structure's resonance frequency through the added-mass effect and dissipates the structure's kinetic energy through viscous losses [38,37].

The fluid dissipation in MEMS is quantified by the quality factor, or Q-factor, Q. The Q-factor is defined as the ratio of the maximum elastic energy stored in the structure E_b per energy dissipated by the fluid in one cycle of oscillation ΔE_f [27] as

$$Q = 2\pi \frac{E_b}{\Delta E_f}. \tag{1}$$

A high Q-factor implies small energy dissipation. For most MEMS applications, high Q-factors are desirable because it leads to an enhanced resonant amplification, thus providing higher signal-to-noise ratio [58].

The most common elastic structures used in micro-resonators are cantilevered slender and thin beams [52,25,29,12,11,35,46,7]. Slender beams are characterized by their in-plane dimensions, where the beam's length is much larger than its width, such that the aspect ratio r_a = length/width is greater than 10. Thinness refers to the beam's thickness being much smaller than its length so that the thickness ratio r_t = thickness/length is smaller than 0.1.

One reason for the use of slender, thin beams for MEMS fluid applications is the existence of several semi-analytical methods to solve for the micro-beam dynamics in viscous fluids. Semi-analytical methods avoid the computational effort associated with the discretization and numerical solution of the beam-fluid interaction problem. Sader [57] proposed a landmark semi-analytical method to determine the steady-state dynamics of a slender micro-beam undergoing out-of-plane displacement in a viscous fluid. In Sader's model, the Euler Bernoulli equation describes the

beam dynamics, and the hydrodynamic force on the beam is calculated by introducing a correction to the drag force on a circular cylinder. Subsequent semi-analytical methods incrementally incorporated more aspects in the scope of the micro-beam fluid interaction problem, e.g., the presence of a nearby rigid wall [5,64,32] or of an elastic surface [17], arrays of beams [12,36,16], torsional modes [64,31,63,1,3], lateral modes [19,10], and fluid compressibility effects [65].

Semi-analytical methods were used extensively to investigate cantilevered micro-beams in both liquids and gases. In water, micro-beams exhibit Q-factor ranging from 1 to 10 in low-order vibrational modes (up to third vibrational mode) [5,7,28,15]. For higher-order modes, Q-factors as high as 30 were obtained [28]. When using slender, thin beams, achieving higher Q-factors (in order of hundreds) for micro-resonator applications in liquids has proven to be a cumbersome task.

Recently it has been discovered experimentally that wide thin plates can exhibit very high Q-factors in liquids. For example, a Q-factor of 197 was obtained in water at 336 kHz when the plate was excited in the so-called roof tile-shaped modes [39,56,47,48]. Roof tile-shaped modes are characterized by having two or more nodal lines parallel to the plate's length ($n_y \geqslant 2$), and only one nodal line parallel to the plate's width ($n_x = 1$), as depicted in Fig. 1. Leissa's nomenclature is particularly useful to classify vibrational modes of plates according to their nodal lines as (n_x, n_y) [41]. In Fig. 1 the first flexural (1,0), the first torsional (1,1), and the first roof tile-shaped (1,2) vibrational modes of a plate are shown.

The application of these high Q-factor vibrational modes of micro-plates in liquids for micro-resonators has been limited due to the complexity of determining the dynamics of micro-plates in viscous fluids. Both fluid dynamics and plate dynamics are more complicated for plates in comparison to beams. For instance, theories such as linear elasticity, a plate theory (e.g., Kirchhoff, Reissner–Mindlin), or shell theory [53] can be used to model the plate dynamics. For any of these theories, numerical techniques are required to solve the plate dynamics when the plate is cantilevered, whereas, for beams, analytical solutions for the Euler–Bernoulli equation are well known [53]. Furthermore, the one-dimensional vibrational modes of beams simplify the fluid flow solution because the fluid velocity at the beam's surface does not vary along the beam's width. A similar simplification can not be implemented for plates since plate modes are intrinsically two-dimensional.

Due to the complexity in solving the micro-plate fluid interaction problem, a few studies favored purely numerical methods[1] [5,56,55,42,24,44,54], instead of semi-analytical approaches. With the purely numerical methods, micro-plates with r_a ranging from 8 to 2 were investigated, and good agreement with experimental data was found. The error in the Q-factor prediction was within 10% for flexural modes [5,44], and within 50% for roof tile-shaped modes [56,55].

The purely numerical methods, although practical, require a fine fluid meshing over a huge volume compared to the size of a fluid mesh cell. What is more, the in-plane dimensions of micro-plates are much larger than the occurring transverse deflections. This multi-scale character of the problem results in discretization requirements that are difficult to fulfill [60]. Furthermore, the pressure gradient near the edges of the micro-plate is high [18], which imposes additional discretization requirements in these regions. These aspects limit the applicability of purely numerical methods

and highlight that a semi-analytic or semi-numeric method for determining the dynamics of micro-plates in viscous fluids is still missing.

Here, we present a semi-numerical method to determine the steady-state dynamics of micro-plate resonators in an incompressible viscous fluid. The proposed method generalizes the existent beam-based semi-analytic methods and, more importantly, overcomes their limitations by accounting for arbitrary two-dimensional plate modes in the structure's dynamics and their effects on the fluid flow. Solving for the dynamics of micro-plates in fluids implies a departure from the assumptions that make the semi-analytic approaches possible. For instance, we model the micro-plate using Kirchhoff plate theory, which requires entirely different solution strategies than existing methods. The resulting equation of motion is solved with a continuous/discontinuous finite element method in which an interior penalty term imposes C^1-continuity to the solution for the plate's deflection. For beams, in comparison, Euler–Bernoulli equation is used, whose analytical solutions are known. The hydrodynamic forces on the plate's surfaces are determined with a boundary integral formulation. For plates, a two-dimensional quadrature scheme for numerically evaluating the hydrodynamic forces is required, whereas for beams, this evaluation is based on an analytical integration [57]. In addition to overcoming a geometric limit of the semi-analytical methods, the present method is also advantageous compared to purely numerical methods. The use of the boundary integral formulation avoids the discretization of the entire fluid domain, which mitigates multi-scale issues, and makes the present method low-costly computationally.

The paper is outlined as follows. In Section 2 a dimensional analysis to delimit the fluid flow regime around micro-plates is presented, followed by the partial differential equations in the time and frequency domain. The semi-numerical method is described in detail in Section 3. One important assumption in the proposed method is that the fluid velocity along the plate's length must be much smaller than in the other directions. This assumption allows the use of a two-dimensional fluid flow formulation which makes the present method very efficient because there are analytical solutions to the arising boundary integrals in each segment of the numerical quadrature scheme [62]. The ramifications due to the two-dimensional flow assumption are discussed in details in Section 3.2, among which we remark that the proposed method is most accurate for low number of nodal lines $n_x \leqslant 6$ and plates with medium aspect ratios $r_a \geqslant 1$. In Section 4, the convergence of the method is discussed, as well as the displacement spectra, quality factors, and mode shapes for structures ranging from slender plates with $r_a = 16$ to a square plate with $r_a = 1$. The last subsections of the paper refer to comparison to results from studies of purely numerical methods, followed by comparison to experimental published results.

2. Statement of the problem

The thickness of the elastic structures used in micro-resonators range from hundreds of nanometers to tens of micrometers, whereas their in-plane dimensions (length and width) vary between tens of micrometers to millimeters [8]. Thin structures with r_t = thickness/length $\leqslant 10$ are common micro-resonator geometries. Thus, a thin plate theory accurately models the elastic structure's dynamics of a wide range of micro-resonators geometries [53][2].

---

[1] Different approaches were used in the purely numerical methods papers. In [5,56,55,42,24] the transient dynamics of the plate is solved with the software ADINA or Comsol Multiphysics when a single vibrational mode is imposed as an initial condition. Maali et al. [44] solved the frequency domain problem by assuming that the plate moved only with flexural beam modes ($n_x, 0$). In [54] the eigenvalue problem is solved with Comsol Multiphysics.

[2] For $r_t \geqslant 10$ a thick plate theory, as Reissner–Mindlin, or the linear elasticity theory can be used to determine the plate's dynamics. However, numerical solutions using Reissner–Mindlin and elasticity theories can be subject to locking-effects in the thin plate limit ($r_t \to 0$), whereas numerical solution of the thin plate theory is not prone to locking-effects [53,13].
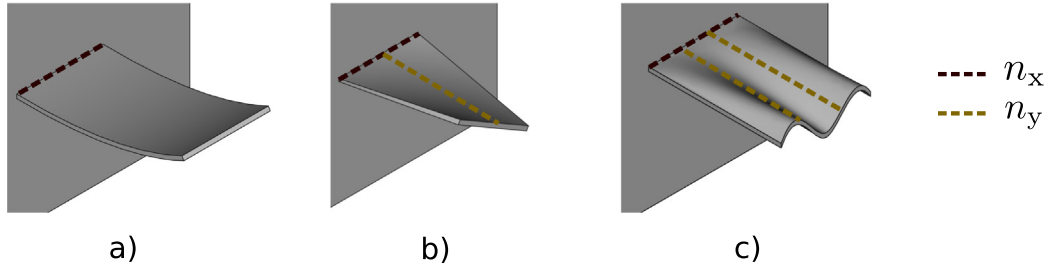
Fig. 1. First a) flexural (1,0), b) torsional (1,1), and c) roof tile-shaped (1,2) vibrational modes of plates. Leissa's nomenclature [41] classifies plate modes as (n_x, n_y), where n_x is the number of nodal lines parallel to the plate's width, and n_y the number of nodal lines parallel to the. plate's length.
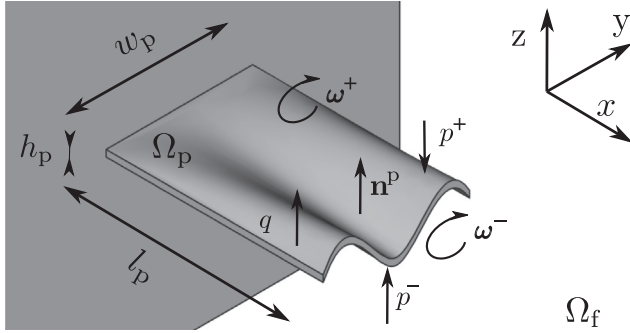

Fig. 2. Thin micro-plate immersed in a viscous fluid and subject to an arbitrary load q. The shown transverse displacement $\phi(x,y)$ of the plate corresponds to the first roof tile-shaped (1,2) vibrational mode.

The elastic structure is a cantilevered thin plate with a uniform width w_p, length l_p and thickness h_p, as shown in Fig. 2. The Cartesian coordinate system has x along the plate's length, y along the plate's width, and z along its thickness. The plate undergoes purely out-of-plane displacement $\phi(x,y)$, while lateral movement in x- and y-directions are negligible. We use the Kirchhoff plate equation for thin plates to determine $\phi(x,y)$, and represent the three-dimensional resonator by its two-dimensional mid-plane Ω_p.

The plate is fully immersed in a fluid of density ρ_f, dynamic viscosity μ_f and kinematic viscosity v_f. The fluid is unbounded, which means the volume of the fluid domain Ω_f is much larger than the volume of the plate and that the fluid velocity far from the plate tends to zero. In addition, the fluid is quiescent, i.e., there is no flow other than the one caused by the plate's movement. These assumptions are typically fulfilled in MEMS applications [57,64,28].

The fluid acts on the plate's surfaces with a pressure p and a vorticity ω. Pressure and vorticity acting on the top plate surface are denoted p^+ and ω^+, respectively. At the bottom plate surface, they are denoted p^- and ω^-, respectively. Since the plate is thin, fluid forces acting on the side surfaces of the plate can be neglected [10]. With the thin plate theory, forces acting on the top and bottom surfaces of the plate are transmitted through the plate without alteration, since the strain of the plate in z-direction is negligible. Thus, the fluid forces acting on the top and bottom plate surfaces can be represented at the plate mid-plane Ω_p.

In the case of a thin micro-plate made of an isotropic material with density ρ_p, Young's Modulus E_p and Poisson's ratio v_p the plate mid-plane dynamics is determined with

$$\frac{E_p I_p}{1 - v_p^2} \left[\frac{\partial^4 \phi}{\partial x^4} + 2 \frac{\partial^4 \phi}{\partial x^2 \partial y^2} + \frac{\partial^4 \phi}{\partial y^4} \right] + \rho_p h_p \frac{\partial^2 \phi}{\partial t^2}$$
$$= q - (p^+ - p^-) \mathbf{n}^p \cdot \mathbf{e}^z + \mu_f [(\boldsymbol{\omega}^+ - \boldsymbol{\omega}^-) \times \mathbf{n}^p] \cdot \mathbf{e}^z, \tag{2}$$

where $I_p = h_p^3/12$ is the moment of inertia of the plate, q is an excitation in z-direction, $\mathbf{n}^p$ is the unit vector normal to the plate's mid-plane and $\mathbf{e}_z$ is the unitary vector in the z-direction $\mathbf{e}_z = (0,0,1)^T$.

The pressure and vorticity differences between the top and bottom surfaces of the plate are denoted as $\Delta p = p^+ - p^-$ and $\Delta \boldsymbol{\omega} = \boldsymbol{\omega}^+ - \boldsymbol{\omega}^-$, respectively. The inner product between $\Delta \boldsymbol{\omega}$ and $\mathbf{e}_z$ in Eq. (2) implies that $\Delta \boldsymbol{\omega}$ is projected onto $\mathbf{e}_z$, i.e., only the z-component of $\Delta \boldsymbol{\omega}$ affect the plate's displacement $\phi(x,y)$.

Silicon is the most common material for MEMS [8], and silicon is an anisotropic material [34], which requires a modification of Eq. (2). The equation of motion of the plate can be rewritten using a material tensor $C_{\alpha\beta\gamma\delta}$ where the indices $\alpha, \beta, \delta, \gamma$ represent x- and y-directions, which yields

$$I_p C_{\alpha\beta\gamma\delta} \phi_{,\alpha\beta\gamma\delta} + \rho_p h_p \frac{\partial^2 \phi}{\partial t^2} = q - \Delta p n_\zeta^p e_\zeta^z + \mu_f \epsilon_{\zeta\tau\xi} \Delta \omega_\zeta n_\tau^p e_\xi^z, \tag{3}$$

where ζ, τ and ξ represent x-, y- and z-directions. The indices following a comma represent spatial derivatives in the index direction, $\epsilon_{\zeta\tau\xi}$ is the Levi–Civita symbol, and $\Delta \omega_\zeta, e_\xi^z$ and n_ζ^p are the components of $\Delta \boldsymbol{\omega}, \mathbf{e}^z$ and $\mathbf{n}^p$, respectively.

The fluid flow around a MEMS resonator can exhibit different regimes. The flow can be in the continuum or the slip flow regime. Moreover, the fluid might be considered compressible or incompressible, depending on the plate dimensions, operating frequency, and fluid properties [37]. The non-dimensional parameters that characterize the fluid flow around a micro-resonator are the Knudsen number Kn, Reynolds number Re and Mach number Ma. Kn is given in terms of Re and Ma as

$$\text{Kn} = \frac{\lambda}{w_p} \sqrt{\frac{\pi \gamma}{2}} \frac{\text{Ma}}{\text{Re}}, \tag{4}$$

where λ is the molecular free path and γ is the ratio of specific heats of the fluid. To define Re and Ma we introduce a characteristic flow velocity u_c, where u_c is the maximum flow velocity at the plate's surface. For a plate vibrating at a single frequency f, u_c is given as $2\pi f \delta$, where δ is the plate's maximum displacement. δ is commonly written as a fraction of the characteristic length as $\delta = \epsilon w_p$. Considering the plate's width w_p as the problem's characteristic length yields[3]

$$\text{Re} = \frac{w_p 2\pi f \delta}{v_f} = \frac{w_p^2 2\pi f \epsilon}{v_f}, \tag{5}$$

and

$$\text{Ma} = \frac{2\pi f \delta}{v_s} = \frac{2\pi f w_p \epsilon}{v_s}, \tag{6}$$

where v_s is the speed of sound in the fluid.

---

[3] The definition of Re in Eq. (5) is similar to studies that focus on beam-fluid interaction with high amplitude displacement [16,24,2,59], while it differs from the non-dimensional number $\beta = 2\pi f w_p^2/v_f$ introduced in some of the other works on beam-fluid interaction by a factor of ϵ [57,64,31].
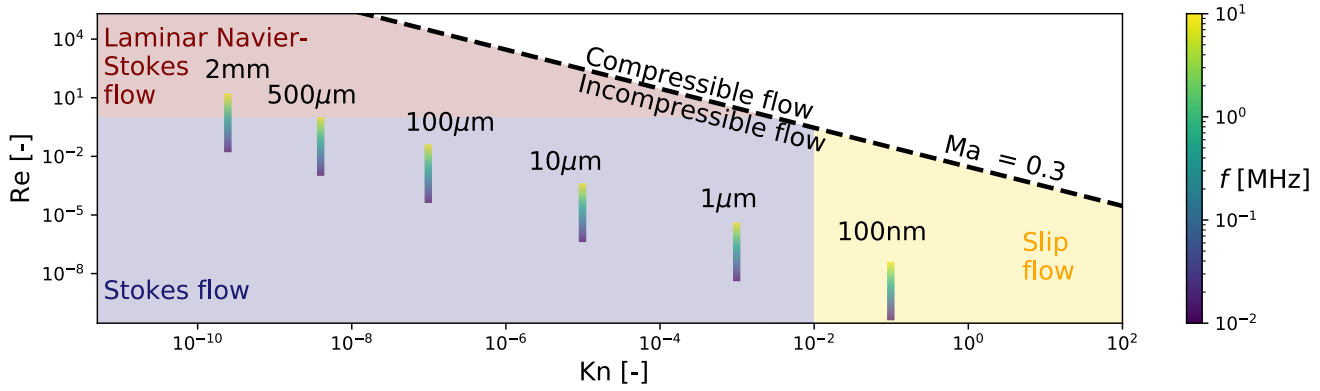
Fig. 3. Classification of the fluid flow around micro-plates in terms of Re and Kn for six characteristic lengths (100 nm, 1 μm, 10 μm, 100 μm, 500 μm, 2 mm). For each length, a rectangle indicates the Re and Kn for a frequency range between 10 kHz and 10 MHz. The color inside the rectangle corresponds to the frequency in the color-bar on the right.

For micro-resonators applications, small amplitude oscillations in the nanometer scale are the most common scenario[4], which results in ϵ in the order of 10^{-6}. Fig. 3 shows that different flow regimes can occur around micro-plates undergoing small amplitude oscillations of $\delta = 10^{-6} w_p$ in air in standard ambient conditions. Slip flow (also called free molecular flow) occurs when Kn $\geqslant 0.01$, where the continuum hypothesis and the no-slip boundary conditions break down. For micro-resonators, Kn is greater than 0.01 only for the narrow plate examples with $w_p = 100$nm. For wider plates with $w_p \geqslant 1$μm, Kn is smaller than 0.01. Hence continuum flow and slip boundary conditions are valid for MEMS resonators with $w_p \geqslant 1$μm in air in ambient conditions. Note that λ is inversely related to pressure, hence in a low vacuum, Kn is larger, and slip flow can be the case even for wider plates depending on the ambient pressure.

Because the continuum model is a valid approach to model the flow around micro-plates, the no-slip and no-penetration boundary conditions are imposed on the surfaces of the plate. Since the plate is very thin, relative motion between the top and bottom surfaces of the plate is neglected. Thus, the fluid velocity **u** at the top and bottom surfaces of the plate are equal to the plate's mid-plane velocity, which yields

$$\mathbf{u} = (u_x, u_y, u_z)^T = \left(0, 0, \frac{\partial \phi}{\partial t}\right)^T. \tag{7}$$

Concerning the fluid compressibility characterization, one condition for incompressibility is a small Mach number Ma $\leqslant 0.3$ [68]. This is usually fulfilled in MEMS due to the small displacement δ. For instance, in Fig. 3 all micro-plates inspected are well below the Ma = 0.3 limit. A second condition for incompressibility of the flow around micro-plates is that the fluid's acoustic wavelength λ_{ac} ($\lambda_{ac} = v_s/f$) must be larger than the plate's flexural wavelength λ_{fl}. For micro-plates in liquids, this condition is fulfilled commonly up to at least 3 MHz [48], and in air up to hundreds of kilohertz [64,65]. Hence, incompressible continuum flow is a standard flow regime around micro-plates. However, since λ_{fl} is mode-dependent, this second incompressibility condition must be checked for each individual vibrational mode.

Incompressible continuum flow can be split in three types: Stokes flow when Re < 1, laminar Navier–Stokes flow for

$1 < $ Re < 4000 and turbulent Navier–Stokes flow at Re > 4000 [37,38][5]. Turbulent flow can occur around MEMS resonators only under exceptional circumstances, such as very large oscillations. The most common flow cases around MEMS are laminar Navier–Stokes flow and Stokes flow. The transition from Stokes flow to laminar Navier–Stokes flow is typically defined at Re = 1 [37,38]. Note in Fig. 3 that the plate with $w_p = 2$mm crosses the limit between laminar Stokes flow (Re < 1) and laminar Navier–Stokes flow (Re > 1) at a frequency around 1 MHz. Above 1 MHz, the convective terms in the Navier–Stokes equations may not be neglected and Stokes equations are not applicable. All smaller plates $w_p \leqslant 500$μm are in the laminar Stokes flow regime up to, at least, 10 MHz. Thus, the flow around micro-plates is typically laminar Stokes flow for plates with width up to hundredths of micrometers, and the unsteady Stokes equations accurately determine the fluid flow around micro-plates.

The unsteady Stokes equations [30] are

$$\frac{\partial \mathbf{u}}{\partial t} = -\frac{1}{\rho_f} \nabla p + v_f \nabla^2 \mathbf{u}, \tag{8}$$

$$\nabla \cdot \mathbf{u} = 0. \tag{9}$$

Eqs. 3, and (7)–(9) form the mathematical model for the micro-plate fluid interaction problem. We focus on periodic solutions of the coupled Eqs. 3, and (7)–(9), whose Fourier transform yields

$$I_p C_{\alpha\beta\gamma\delta} \hat{\phi}_{,\alpha\beta\gamma\delta} - \omega^2 \rho_p h_p \hat{\phi} = \hat{q} - \Delta \hat{p} n_\zeta^p e_\zeta^z + \mu_f \epsilon_{\zeta\tau\xi} \Delta \hat{\omega}_\zeta n_\tau^p e_\xi^z, \tag{10}$$

$$j\omega \hat{\mathbf{u}} = -\frac{1}{\rho_f} \nabla \hat{p} + v_f \nabla^2 \hat{\mathbf{u}}, \tag{11}$$

$$\nabla \cdot \hat{\mathbf{u}} = 0, \tag{12}$$

$$\hat{\mathbf{u}}|_{\Omega_p} = \left(0, 0, j\omega \hat{\phi}\right)^T, \tag{13}$$

where j is the imaginary unity. Since the Eqs. 3, and (7)–(9) are linear, their Fourier transforms do not contain coupling terms between different frequencies. $\hat{\phi}, \hat{q}, \hat{\mathbf{u}}, \hat{\omega}$ and $\hat{p}$ refer to the Fourier transform of the time-dependent quantities $\phi, q, \mathbf{u}, \omega$ and p.

3. Numerical method

An analytic solution to the Kirchhoff plate equation with cantilevered boundary conditions is not known [53]. We use finite element method (FEM) to determine the plate dynamics numerically. In the following sections, the implementation of the plate continuity conditions and the coupling between fluid and plate are discussed. The numerical method was implemented with the Finite Element (FE) package FEniCS [43].

---

[4] Some MEMS applications as micro-fanning [14,23,33] and robotic propulsion [7] can make use of high amplitude oscillations.

[5] The transition Re = 4000 from laminar to turbulent flow was taken from the flow in long channels of circular cross-section as there is not a clear transition specified for micro-structures in fluids [37,38]

3.1. Interior Penalty Method

The boundaries of the plate's mid-plane Ω_p are denoted by $\partial\Omega_p$, which is formed by the union of the clamped edge boundary Γ_c with the free edge boundary $\Gamma_f, \Gamma_c \cup \Gamma_f = \partial\Omega_p$. The intersection of Γ_c and Γ_f are denoted $c, \Gamma_c \cap \Gamma_f = c$, as depicted in Fig. 4a).

The plate is cantilevered, which means it is clamped at one side where $x = 0$ and free at all other sides. Clamped and free edge boundary conditions are defined in index notation as

$$\left.\begin{array}{ll} \hat{\phi} &= 0 \\ \hat{\phi}_{,\alpha} n_\alpha &= 0 \end{array}\right\} \quad \text{on } \Gamma_c, \tag{14}$$

and

$$\left.\begin{array}{ll} I_p C_{\alpha\beta\gamma\delta} \hat{\phi}_{,\gamma\delta} n_\alpha n_\beta &= 0 \\ I_p C_{\alpha\beta\gamma\delta} \hat{\phi}_{,\beta\gamma\delta} n_\alpha + I_p \left(C_{\alpha\beta\gamma\delta} \hat{\phi}_{,\gamma\delta} s_\alpha n_\beta \right)_{,s} &= 0 \end{array}\right\} \quad \text{on } \Gamma_f, \tag{15}$$

respectively. n_α and s_α denote the components of the unit outward normal and the unit tangent vectors at the boundaries $\partial\Omega_p$, respectively. Force equilibrium on the plate's corners is imposed with

$$I_p C_{\alpha\beta\gamma\delta} \hat{\phi}_{,\gamma\delta} s_\alpha n_\beta|_{c^+} - I_p C_{\alpha\beta\gamma\delta} \hat{\phi}_{,\gamma\delta} s_\alpha n_\beta|_{c^-} = 0, \quad \forall c, \tag{16}$$

where $c^\pm$ are the two nearest neighbor points on the two edges that meet at the corner c, infinitesimally near the corner c [67].

The numerical solution of Eq. (10) using FEM requires the solution function space to be H^2, i.e., the Sobolev space of functions with square-integrable generalized second derivatives. This means C^1 continuity of the basis functions in the solution function space is required, so that no discontinuities in the slope of the displacement $\hat{\phi}$ exist, as such discontinuities are unphysical. C^1 continuous basis functions in two dimensions are very challenging to implement [4]. An alternative to C^1 basis functions are continuous/discontinuous Galerkin methods [4,9,40,21]. Continuous/discontinuous methods combine standard Lagrangian C^0 continuous basis functions with discontinuous methods such as interior penalty (IP) methods [4,21,22] or lifting methods [67,6,20,45] to enforce C^1 continuity of the solution. In this work, we implement an IP method, which is consistent, stable, convergent, and can be implemented using standard FE packages [21,22].

We consider a partitioning of the plate's mid-plane $\mathcal{P}(\Omega_p)$ in triangular elements $E_i, i = 1, \ldots, \mathcal{N}_y \times \mathcal{N}_x$, where $\mathcal{N}_y$ and $\mathcal{N}_x$ are the number of elements in y- and x-direction, respectively[6]. The union of all internal edges e_i is denoted by $\tilde{\Gamma}$, and the union of internal edges and external boundaries is denoted by $\Gamma = \tilde{\Gamma} \cup \partial\Omega_p$.

To obtain the weak form of Eq. (10), the function space $\mathcal{W}^h$ is defined using the partitioning $\mathcal{P}(\Omega_p)$ as

$$\mathcal{W}^h = \left\{ \hat{\phi}^h \in H^2(\Omega_p) : \hat{\phi}^h|_{E_i} \in P^k(E_i) \forall E_i \in \mathcal{P}(\Omega_p), \hat{\phi}^h|_{\Gamma_c} = 0 \right\}, \tag{17}$$

where $P^k(E_i)$ are C^0 Lagrangian FE shape functions of degree k defined on the element E_i. The Dirichlet boundary condition at Γ_f appears as a direct restriction of the function space $\mathcal{W}^h$.

To account for discontinuities in the FE solution, the average $\langle \cdot \rangle$ and the jump $[[\cdot]]$ operators are introduced. For two internal elements E^+ and E^- as shown in Fig. 4b) the average operator of the derivative of a scalar function a in the direction α at the edge e_i is

$$\langle a_{,\alpha} \rangle = 1/2 \left(a_{,\alpha}^+ + a_{,\alpha}^- \right), \tag{18}$$

---

[6] An structured mesh is considered because of its simplicity, but any unstructured mesh could be used without loss of generality.

where the $+$ and $-$ superscripts mean evaluation at the edge e_i in the elements E^+ and E^-, respectively. The jump of the derivative of a in the normal direction at e_i is

$$[[a_{,n}]] = a_{,\alpha}^+ n_\alpha^+ + a_{,\alpha}^- n_\alpha^-. \tag{19}$$

The discretized weak form of Eq. (10) is obtained by multiplying Eq. (10) with a test function $w^h \in \mathcal{W}^h$, replacing $\hat{\phi}$ by an FE approximation $\hat{\phi}^h \in \mathcal{W}^h$ and integrating over the domain Ω_p, which yields

$$\begin{aligned} &\int_{\Omega_p} I_p C_{\alpha\beta\gamma\delta} \hat{\phi}_{,\alpha\beta\gamma\delta}^h w^h \, d\Omega - \int_{\Omega_p} \omega^2 \rho_p h_p \hat{\phi}^h w^h \, d\Omega \\ &= \int_{\Omega_p} \hat{q} w^h \, d\Omega - \int_{\Omega_p} \Delta\hat{p} n_\zeta^p e_\zeta^z w^h \, d\Omega \\ &+ \int_{\Omega_p} \mu_f \epsilon_{\zeta\tau\xi} \Delta\hat{\omega}_\zeta n_\tau^p e_\xi^z w^h \, d\Omega, \quad \forall w^h \in \mathcal{W}^h. \end{aligned} \tag{20}$$

The first term in Eq. (20) is integrated twice by parts accounting for shear force and moment boundary conditions, which renders

$$\begin{aligned} &\int_{\Omega_p} I_p C_{\alpha\beta\gamma\delta} \hat{\phi}_{,\alpha\beta}^h w_{,\gamma\delta}^h d\Omega - \\ &\int_{\tilde{\Gamma}\cup\Gamma_c} I_p \left[\!\left[C_{\alpha\beta\gamma\delta} w_{,\alpha}^h n_\beta \right]\!\right] \left\langle \hat{\phi}_{,\gamma\delta}^h n_\gamma n_\delta \right\rangle d\Gamma \\ &- \int_{\tilde{\Gamma}\cup\Gamma_c} I_p \left[\!\left[C_{\alpha\beta\gamma\delta} \hat{\phi}_{,\alpha}^h n_\beta \right]\!\right] \left\langle w_{,\gamma\delta}^h n_\gamma n_\delta \right\rangle d\Gamma \\ &+ \int_{\tilde{\Gamma}\cup\Gamma_c} I_p \frac{\tau}{h_E} C_{\alpha\beta\gamma\delta} \left[\!\left[\hat{\phi}_{,\beta}^h n_\beta \right]\!\right] \left[\!\left[w_{,\gamma}^h n_\delta \right]\!\right] d\Gamma \\ &- \int_{\Omega_p} \omega^2 \rho_p h_p \hat{\phi}^h w^h d\Omega \\ &= \int_{\Omega_p} \hat{q} w^h d\Omega - \int_{\Omega_p} \Delta\hat{p} n_\zeta^p e_\zeta^z w^h d\Omega \\ &+ \int_{\Omega_p} \mu_f \epsilon_{\zeta\tau\xi} \Delta\hat{\omega}_\zeta n_\tau^p e_\xi^z w^h d\Omega, \quad \forall w^h \in \mathcal{W}^h, \end{aligned} \tag{21}$$

where h_E is the diameter of the inner elements E_i. The first and second terms on the left-hand-side (LHS) of Eq. (21) are obtained directly from the integration by parts of Eq. 20. The third term to the LHS of Eq. (20) was added so that the method yields a symmetric bilinear form. The fourth term on the LHS is the penalisation term, which ensures $\left[\!\left[\hat{\phi}_{,\alpha}^h n_\beta \right]\!\right] \to 0$ for a suitable τ and imposes C^1 continuity of $\hat{\phi}^h$ and w^h [22]. The slope boundary condition is weakly imposed with the integral of the third and fourth terms of the LHS on Γ_c. No explicit terms of vertex terms for the corner forces are necessary since the corner forces equilibrium is automatically fulfilled [22,67]. The value of τ has to be determined empirically such that the method is convergent [4,22,26]. The procedure for determining τ is discussed in Section 4.1.

3.2. Boundary integral method

The unsteady Stokes equations (Eqs. 11 and 12) are solved using the boundary integral method. With the boundary integral
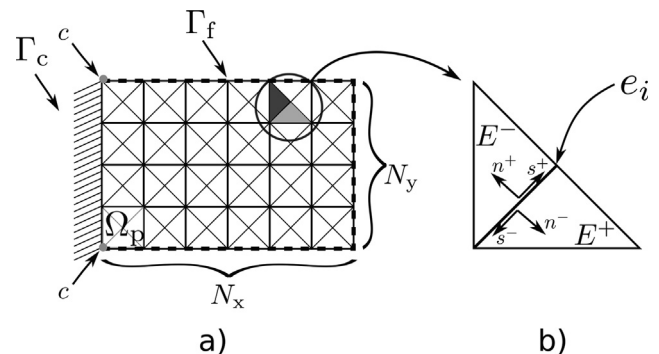

Fig. 4. a) Partitioning of the plate's mid surface Ω_p in N_x by N_y elements. Left boundary Γ_c is clamped, all others are free Γ_f (dashed line) and gray dots are the corners c intersecting Γ_f and Γ_c. b) Close-up view of two neighbouring elements E^- and E^+ sharing an internal edge e_i. $\mathbf{n}^\pm$ and $\mathbf{s}^\pm$ are the normal and tangent vectors at the edge e_i from element $E^\pm$ to $E^\mp$.

method, the fluid forces acting on the plate's surface are calculated using the fundamental solution to the unsteady Stokes equations, without the necessity for discretizing and numerically solving the unsteady Stokes equations in the entire fluid domain Ω_f. The unsteady Stokes equations have different fundamental solutions, e.g., the Stokeslet in two or three dimensions [50,51] and the fundamental solution to the stream-function formulation of the unsteady Stokes equations in two dimensions. One advantage of the latter fundamental solution is that analytical solutions to the arising boundary integrals were obtained [62].

Due to the efficiency of the latter approach, the majority of the semi-analytical models for micro-beams in viscous fluids solves a boundary integral assuming two-dimensional fluid flow around the beam [57,32,36,31,63,1,3,19,10]. A two-dimensional fluid flow is confined in a plane. In the semi-analytic models discussed, this plane is parallel to the y-z plane, as shown in Fig. 5a. Thus the fluid moves only in y- and z-directions.

The exact extent to which three-dimensional flow affects the beam's and plate's dynamics in fluids is yet an unsolved question [7,5,42,24]. Comparison to purely numerical methods [42,24] show that a two-dimensional flow formulation accurately predicts the pressure acting on the plate everywhere except near the plate's completely free edge at $x = l_\text{p}$ [24]. Near the plate's free edge, the two-dimensional fluid model overestimates the pressure because the fluid is forced to move farther in the direction of the side edges of the plates ($y = \pm w_\text{p}/2$) instead of moving over the completely free edge of the plate ($x = l_\text{p}$). As a consequence, the use of two-dimensional fluid flow approximation underestimates both the plate's resonance frequency and the Q-factor in comparison to purely numerical predictions. These differences were found to be smaller than 5% for low order vibrational modes ($n_\text{x} \leqslant 3$), and increase with n_x up to 20% in the sixth flexural mode ($n_\text{x} = 6$) [5].

Here, the viscous flow is modeled with the two-dimensional fundamental solution to the stream-function formulation. This formulation makes the present method very efficient. However, it imposes two main limitations for the methods applicability. The plate's aspect ratio r_a must be greater than 1, so that the fluid flow over the entirely free edge of the plate does not dominate the fluid flow. Secondly, n_x must be smaller than 6, because u_x increases with the number of nodal lines n_x.

To solve the micro-plate fluid interaction problem with the boundary integral method using the two-dimensional fundamental solution, the stream-function formulation in vector notation in frequency domain is introduced. The fluid velocity along the x-axis is assumed to be negligible $\hat{\mathbf{u}}^T = (0, \hat{u}_\text{y}, \hat{u}_\text{z})$, as well as the variation of the fluid velocity along the x-axis $\partial \hat{\mathbf{u}}^T / \partial x = (0, 0, 0)$. The vorticity vector $\hat{\omega}$ is given by

$$\hat{\omega} = \nabla \times \hat{\mathbf{u}}, \tag{22}$$

and the vector potential $\hat{\psi}$

a)   b)

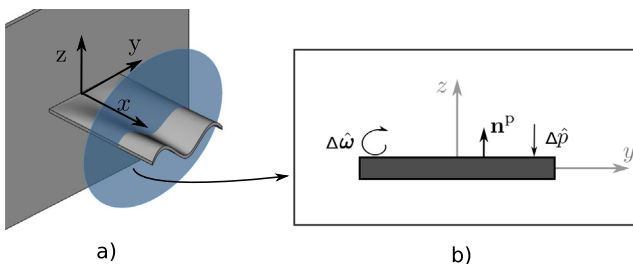**Fig. 5.** a) The fluid flow is confined to a plane (in blue), which is parallel to the plate's cross-section. b) Vorticity $\Delta\hat{\omega}$ and pressure $\Delta\hat{p}$ differences act on the plate. The equilibrium configuration of the plate is a flat surface, and $\mathbf{n}^\text{p}$ is parallel to the z-direction.

$$\hat{\mathbf{u}} = \nabla \times \hat{\psi}. \tag{23}$$

Using the definition from Eq. (23) in Eq. (22) leads to

$$\hat{\omega} = -\nabla^2 \hat{\psi}. \tag{24}$$

Taking the curl of Eq. (11) and writing the vorticity $\hat{\omega}$ in terms of the vector potential $\hat{\psi}$ yields

$$\nabla^4 \hat{\psi} - \frac{\text{j}\omega}{v_\text{f}} \nabla^2 \hat{\psi} = (0, 0, 0)^T. \tag{25}$$

The vector potential that satisfies Eq. (25), satisfies both Eq. (11) and Eq. (12). Since the velocity in x-direction and fluid velocity $\hat{\mathbf{u}}$ variations in x-direction are negligible, the vorticity has only one non-zero component, $\hat{\omega}^T = (\hat{\omega}_\text{x}, 0, 0)$, which implies $\hat{\psi}^T = (\hat{\psi}_\text{x}, 0, 0)$. $\hat{\psi}_\text{x}$ is the stream-function for the two-dimensional flow field. The fundamental solution $\hat{\Psi}$ to the x-component of Eq. (25) is defined as [62]

$$\hat{\Psi} = \frac{1}{2\pi} \frac{v_\text{f}^2}{\omega^2} \left\{ \log\left(\sqrt{(y-y')^2 + (z-z')^2}\right) + K_0\left(\text{j}\omega \sqrt{(y-y')^2 + (z-z')^2}\right) \right\}, \tag{26}$$

where K_0 is the modified Bessel function of the third kind and order zero. y' and z' are coordinate axes with coincident orientation to y and z, respectively.

The fundamental solution $\hat{\Psi}$ can be used to describe the fluid forces at the plate's surfaces. Since the plate is a thin structure, consistently the plate domain is represented by its two-dimensional mid-plane Ω_p [62,50,51]. The vorticity difference $\Delta\hat{\omega}$ has only one non-zero component, i.e., $\Delta\hat{\omega} = (\Delta\hat{\omega}_\text{x}, 0, 0)^T$. With the application of Green's theorem at Ω_p, $\hat{\psi}_\text{x}$ is determined at a position x as a function of $\Delta\hat{\omega}_\text{x}$ and $\Delta\hat{p}$ with

$$\hat{\psi}_\text{x}(x, y', z') = \int_{-w_\text{p}/2}^{w_\text{p}/2} \Delta\hat{\omega}_\text{x}(x, y) \frac{\partial \hat{\Psi}}{\partial n} - \frac{1}{\mu_\text{f}} \Delta\hat{p}(x, y) \frac{\partial \hat{\Psi}}{\partial s} \, ds, \tag{27}$$

where the derivative with respect to n is derivative in the direction of the surface normal $\mathbf{n}^\text{p}$ and the derivative with respect to s is the tangential derivative on Ω_p along the plate's width. We assume the equilibrium configuration of Ω_p in the absence of external forces and internal stress to be a flat surface. With this equilibrium configuration, $\mathbf{n}^\text{p}$ is parallel to the z-direction as shown in Fig. 5, ergo $n = z$ and $s = y$ at the plate's mid-plane $z = 0$, which yields

$$\hat{\psi}_\text{x}(x, y', z') = \int_{-w_\text{p}/2}^{w_\text{p}/2} \Delta\hat{\omega}_\text{x}(x, y) \left.\frac{\partial \hat{\Psi}}{\partial z}\right|_{z=0} - \frac{1}{\mu_\text{f}} \Delta\hat{p}(x, y) \left.\frac{\partial \hat{\Psi}}{\partial y}\right|_{z=0} \, dy. \tag{28}$$

Differentiation of Eq. (28) with respect to y' renders a relation between $\Delta\hat{\omega}_\text{x}$ and $\Delta\hat{p}$ with $\hat{u}_\text{z}$ at the plate's mid-plane $z' = 0$ as

$$\hat{u}_\text{z}(x, y', 0) = -\int_{-w_\text{p}/2}^{w_\text{p}/2} \Delta\hat{\omega}_\text{x}(x, y) \left.\frac{\partial^2 \hat{\Psi}}{\partial z \partial y'}\right|_{\substack{z=0 \\ z'=0}} dy$$
$$+ \frac{1}{\mu_\text{f}} \int_{-w_\text{p}/2}^{w_\text{p}/2} \Delta\hat{p}(x, y) \left.\frac{\partial^2 \hat{\Psi}}{\partial y \partial y'}\right|_{\substack{z=0 \\ z'=0}} dy. \tag{29}$$

Knowing that $\partial^2\hat{\Psi}/\partial z \partial y' = 0$ at $z = z' = 0$ [62] and applying the no-penetration boundary condition, defined in Eq. (13), renders a relation between $\Delta\hat{p}$ and the plate's transverse displacement $\hat{\phi}$ as

$$\int_{-w_\text{p}/2}^{w_\text{p}/2} \Delta\hat{p}(x, y) \left.\frac{\partial^2 \hat{\Psi}}{\partial y \partial y'}\right|_{\substack{z=0 \\ z'=0}} dy = \mu_\text{f} \text{j}\omega \hat{\phi}(x, y'). \tag{30}$$

Note that the function $\partial^2\hat{\Psi}/\partial y \partial y'$ relates the pressure difference at a point x, y with the displacement at another point x, y' in the same cross-section at a position x.

Differentiating Eq. (28) with respect to z', and knowing that the term $\partial^2\hat\Psi/\partial z\partial z'$ vanishes at $z = z' = 0$ [62], renders

$$\int_{-w_{\mathrm{p}}/2}^{w_{\mathrm{p}}/2} \Delta\hat\omega_{\mathrm{x}}(x,y)\left.\frac{\partial^2\hat\Psi}{\partial y\partial z'}\right|_{\substack{z=0\\z'=0}} \mathrm{d}y = \hat u_{\mathrm{y}}(x,y',0), \tag{31}$$

where $\hat u_{\mathrm{y}}$ is the y-component of the fluid velocity at Ω_{p}. From the no-slip boundary condition in Eq. (13), $\hat u_{\mathrm{y}} = 0$, which implies $\Delta\hat\omega_{\mathrm{x}} = 0$, and therefore $\Delta\hat{\boldsymbol\omega} = (0,0,0)^T$. Hence, in the absence of lateral plate movements, the vorticity jump at the plate does not influence the fluid flow field, nor the plate's dynamics, and the vorticity term in the weak form in Eq. (21) of the Kirchhoff equation is zero.

3.3. Chebyshev-Gauss quadrature

The finite element approximation of the weak form in Eq. (21) requires the projection of the pressure difference $\Delta\hat p$ onto the functions space $\mathcal{W}^{\mathrm{h}}$. With the equilibrium configuration discussed in Section 3.2, $\mathbf{n}^{\mathrm{p}} = \mathbf{e}^{\mathrm{z}}$, and the inner product $n_\zeta^{\mathrm{p}}e_\zeta^{\mathrm{z}}$ in Eq. (21) equals to 1. Hence, integration of $\Delta\hat p$ over the domain Ω_{p} yields simply

$$\int_{\Omega_{\mathrm{p}}} \Delta\hat p n_\zeta^{\mathrm{p}}e_\zeta^{\mathrm{z}} w^{\mathrm{h}}\mathrm{d}\Omega = \int_{\Omega_{\mathrm{p}}} \Delta\hat p\, w^{\mathrm{h}}\mathrm{d}\Omega. \tag{32}$$

In this subsection, a numerical procedure to evaluate the integral in Eq. (32) using the pressure difference definition in Eq. (30) is introduced.

3.3.1. 1D Integration

To numerically solve Eq. (30) for the pressure difference $\Delta\hat p$ it is crucial to understand how the terms $\Delta\hat p$ and $\partial^2\hat\Psi/\partial y\partial y'$ behave. The pressure difference $\Delta\hat p$ over a ribbon moving with uniform velocity $\hat u_{\mathrm{z}}$ is unbounded at the edges $y = \pm w_{\mathrm{p}}/2$ and exhibits an inverse square-root singularity towards the edges [62]. This singularity also occurs when the plate moves with a non-uniform velocity $\hat u_{\mathrm{z}} = \hat u_{\mathrm{z}}(x,y)$. $\partial^2\hat\Psi/\partial y\partial y'$ exhibits a logarithmic singularity for $|y - y'| \to 0$, and oscillates while decaying to zero for $|y - y'| \to \infty$ [62].

Numerical integration of the LHS of Eq. (30) requires considering a suitable quadrature scheme for the inverse square-root singularity of $\Delta\hat p$. An appropriate choice of quadrature scheme is the Chebyshev-Gauss quadrature. In y-direction, the Chebyshev-Gauss quadrature points are distributed over the plate's width as

$$y_i = \frac{w_{\mathrm{p}}}{2}\cos\left(\frac{2i-1}{2\mathcal{N}_{\mathrm{y}}}\pi\right), \tag{33}$$

where $\mathcal{N}_{\mathrm{y}}$ is the number of grid points in the y-direction and $i = 1\ldots b\mathcal{N}_{\mathrm{y}}$. With such quadrature scheme, the variation of $\Delta\hat p$ between two grid points is much smaller than the variation of $\partial^2\hat\Psi/\partial y\partial y'$ in the same segment [62]. The numerical integration of the LHS of Eq. (30) becomes a sum of $\mathcal{N}_{\mathrm{y}}$ integrals as

$$\sum_{i=1}^{\mathcal{N}_{\mathrm{y}}}\Delta\hat p(x,y_i)\int_{y_i^{(\mathrm{l})}}^{y_{i+1}^{(\mathrm{l})}}\frac{\partial^2\hat\Psi}{\partial y\partial y'}\mathrm{d}y = \mu_{\mathrm{f}}\mathrm{j}\omega\hat\phi\left(x,y_j'\right) \tag{34}$$

where the pressure difference $\Delta\hat p(x,y_i)$ and the displacement $\hat\phi\left(x,y_j'\right)$ are discretized in y-direction according to Eq. (33). The limits of integration $y_j^{(\mathrm{l})}$ and $y_{j+1}^{(\mathrm{l})}$ are defined as $y^{(\mathrm{l})} = [-w_{\mathrm{p}}/2,\ldots by_i/2 + y_{i+1}/2\ldots bw_{\mathrm{p}}/2]$, where $y^{(\mathrm{l})}$ has $\mathcal{N}_{\mathrm{y}} + 1$ points, as shown in Fig. 6.

For each integral in Eq. (34), there exists an analytical solution [62] given by

$$\int_{y_i^{(\mathrm{l})}}^{y_{i+1}^{(\mathrm{l})}}\frac{\partial^2\Psi}{\partial y\partial y'}\mathrm{d}y = \frac{\sqrt{v_{\mathrm{f}}}}{\mathrm{j}2\pi\sqrt\omega}\left[\mathcal{F}\left(\sqrt{\frac{\omega}{v_{\mathrm{f}}}}\left(y_{i+1}^{(\mathrm{l})} - y_j'\right)\right)\right.$$
$$\left. -\mathcal{F}\left(\sqrt{\frac{\omega}{v_{\mathrm{f}}}}\left(y_i^{(\mathrm{l})} - y_j'\right)\right)\right]. \tag{35}$$

Evaluation of Eq. (35) depends on the position y_j' as well as on the limits of integration $y_{i+1}^{(\mathrm{l})}$ and $y_i^{(\mathrm{l})}$. The function $\mathcal{F}$ is defined as

$$\mathcal{F}(g) = \frac{1}{g} + \frac{\mathrm{dKer}(g)}{\mathrm{d}g} + \mathrm{j}\frac{\mathrm{dKei}(g)}{\mathrm{d}g} \quad \text{for}\quad g > 0, \tag{36}$$

$$\mathcal{F}(g) = \frac{1}{g} - \frac{\mathrm{dKer}(-g)}{\mathrm{d}g} - \mathrm{j}\frac{\mathrm{dKei}(-g)}{\mathrm{d}g} \quad \text{for}\quad g < 0, \tag{37}$$

where $\mathrm{dKer}/\mathrm{d}g$ and $\mathrm{dKei}/\mathrm{d}g$ are the first derivatives of the real and imaginary Kelvin Functions, respectively.

Eq. (34) is written as a matrix–vector product,

$$\mathbf{A}\Delta\hat{\mathbf{p}} = \mu_{\mathrm{f}}\mathrm{j}\omega\hat{\boldsymbol\phi}. \tag{38}$$

The matrix elements A_{ij} are given by the right-hand-side (RHS) of Eq. (35) as

$$A_{ij} = \frac{\sqrt{v_{\mathrm{f}}}}{\mathrm{j}2\pi\sqrt\omega}\left[\mathcal{F}\left(\sqrt{\frac{\omega}{v_{\mathrm{f}}}}\left(y_{i+1}^{(\mathrm{l})} - y_j'\right)\right) - \mathcal{F}\left(\sqrt{\frac{\omega}{v_{\mathrm{f}}}}\left(y_i^{(\mathrm{l})} - y_j'\right)\right)\right]. \tag{39}$$

$\Delta\hat{\mathbf{p}}$ and $\hat{\boldsymbol\phi}$ are the pressure difference and displacement vectors evaluated at all points y_j at the same cross-section at a fixed x. Multiplying Eq. (38) with the inverse matrix $\mathbf{A}^{-1}$, a matrix–vector product for the pressure difference $\Delta\hat{\mathbf{p}}$ is obtained as

$$\Delta\hat{\mathbf{p}} = \mu_{\mathrm{f}}\mathrm{j}\omega\mathbf{A}^{-1}\hat{\boldsymbol\phi}. \tag{40}$$
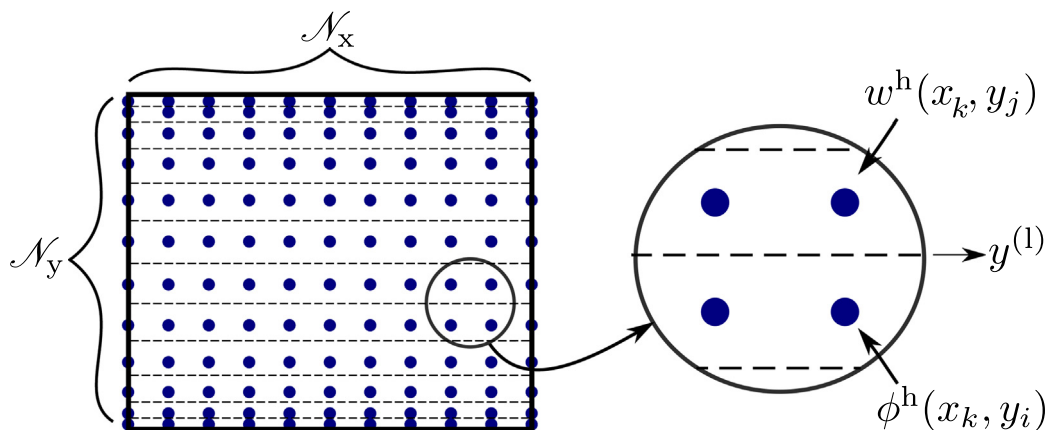

Fig. 6. Fluid grid with $\mathcal{N}_{\mathrm{y}}$ by $\mathcal{N}_{\mathrm{x}}$ grid points. Dashed lines represent limits $y^{(\mathrm{l})}$ in y-direction.

3.3.2. Projection onto $\mathcal{W}^h$

Since a two-dimensional formulation for the fluid dynamics is implemented, the pressure difference $\Delta\hat{p}(x,y)$ depends only on the displacements $\hat{\phi}(x,y)$ on the same position x. Integration of the pressure difference $\Delta\hat{p}$ in Eq. (32) is written as successive integration in y and x-direction as

$$\int_{\Omega_p} \Delta\hat{p}(x,y)\, w^h d\Omega = \int_0^{l_p}\int_{-w_p/2}^{w_p/2}\Delta\hat{p}(x,y)\, w^h(x.y)\mathrm{d}y\mathrm{d}x. \quad (41)$$

Numerical evaluation of the integral in x-direction is achieved with the Simpson's one-third rule as

$$\int_{\Omega_p}\Delta\hat{p}(x,y)\, w^h d\Omega \approx \sum_{k=1}^{\mathcal{N}_x}\varpi_k\int_{-w_p/2}^{w_p/2}\Delta\hat{p}(x_k,y)\, w^h(x_k,y)\mathrm{d}y, \quad (42)$$

where w_k are the Simpson's rule weighting constants. With the Simpson's one-third rule $\mathcal{N}_x$ must be an odd number.

To evaluate the y-integration of $\Delta\hat{p}(x_k,y)$ note that the integration of a polynomial function f divided by the inverse square root singularity with Chebyshev-Gauss quadrature is given by

$$\int_{-w_p/2}^{w_p/2}\frac{f(y)}{\sqrt{\left(w_p/2\right)^2 - y^2}}\mathrm{d}y = \frac{\pi}{n}\sum_{j=1}^n f(y_j), \quad (43)$$

where $f(y_j)$ are the function's value at the discrete points defined in Eq. (33). The definition in 43 is exact when the degree of the polynomial function f is $n-1$. This definition is used to numerically evaluate the integral of $\Delta\hat{p}(x_k,y)$ in y-direction in Eq. (42) as

$$\int_{\Omega_p}\Delta\hat{p}(x,y)\, w^h d\Omega \approx \sum_{k=1}^{\mathcal{N}_x}\varpi_k\sum_{j=1}^{\mathcal{N}_y}\frac{\pi}{\mathcal{N}_y}\Delta\hat{p}(x_k,y_j) \\ w^h(x_k,y_j)\sqrt{\left(w_p/2\right)^2 - y_j^2}. \quad (44)$$

The union of all points (x_k,y_j) and (x_k,y_j) form the fluid grid, which is represented in Fig. 6. In essence the fluid grid consists of $\mathcal{N}_x$ cross-sections parallel to y linearly spaced in the x-direction from $x=0$ to $x=l_p$, and $\mathcal{N}_y$ grid points in y-direction positioned according to Eq. (33).

To determine $\Delta\hat{p}(x_k,y_j)$, Eq. (40) is rewritten in summation notation as

$$\Delta\hat{p}(x_k,y_j) = \mu_f\mathrm{j}\omega\sum_{i=1}^{\mathcal{N}_y}A_{ij}^{-1}\hat{\phi}(x_k,y_i), \quad (45)$$

and using this definition in Eq. (44) yields

$$\int_{\Omega_p}\Delta\hat{p}(x,y)\, w^h d\Omega = \mu_f\mathrm{j}\omega\frac{\pi}{\mathcal{N}_y}\sum_{k=1}^{\mathcal{N}_x}\varpi_k\sum_{j=1}^{\mathcal{N}_y}\sum_{i=1}^{\mathcal{N}_y}A_{ij}^{-1}\hat{\phi}^h(x_k,y_i) \\ w^h(x_k,y_j)\sqrt{\left(w_p/2\right)^2 - y_j^2}. \quad (46)$$

Eq. (46) reveals that the projection of the pressure difference corresponds to a weighted projection of the inverse of matrix $\mathbf{A}^{-1}$ into the function space $\mathcal{W}^h$.

With the projection of $\Delta\hat{p}(x,y)$ into $\mathcal{W}^h$ as defined in Eq. (46), and neglecting the vorticity term as discussed in Section 3.2, the equation of motion of the plate in a viscous fluid from Eq. (21) is rewritten as

$$\int_{\Omega_p}I_p C_{\alpha\beta\gamma\delta}\hat{\phi}_{,\alpha\beta}^h w_{,\gamma\delta}^h d\Omega$$
$$-\int_{\tilde{\Gamma}\cup\Gamma_c}I_p\left[\!\left[C_{\alpha\beta\gamma\delta}w_{,\alpha}^h n_\beta\right]\!\right]\left\langle\hat{\phi}_{,\gamma\delta}^h n_\gamma n_\delta\right\rangle\mathrm{d}\Gamma$$
$$-\int_{\tilde{\Gamma}\cup\Gamma_c}I_p\left[\!\left[C_{\alpha\beta\gamma\delta}\hat{\phi}_{,\alpha}^h n_\beta\right]\!\right]\left\langle w_{,\gamma\delta}^h n_\gamma n_\delta\right\rangle\mathrm{d}\Gamma$$
$$+\int_{\tilde{\Gamma}\cup\Gamma_c}I_p\frac{\tau}{h_E}C_{\alpha\beta\gamma\delta}\left[\!\left[\hat{\phi}_{,\alpha}^h n_\beta\right]\!\right]\left[\!\left[w_{,\gamma}^h n_\delta\right]\!\right]\mathrm{d}\Gamma$$
$$-\int_{\Omega_p}\omega^2\rho_p h_p\hat{\phi}^h w^h d\Omega$$
$$+\mu_f\mathrm{j}\omega\frac{\pi}{\mathcal{N}_y}\sum_{k=1}^{\mathcal{N}_x}\varpi_k\sum_{j=1}^{\mathcal{N}_y}$$
$$\sum_{i=1}^{\mathcal{N}_y}\mathbf{A}_{ij}^{-1}\hat{\phi}^h(x_k,y_i)\, w^h(x_k,y_j)\sqrt{\left(w_p/2\right)^2 - y_j^2}$$
$$= \int_{\Omega_p}\hat{q}\, w^h d\Omega, \quad\forall w^h\in\mathcal{W}^h. \quad (47)$$

The proposed method is resumed to a single equation to determine the plate dynamics, which accounts for the viscous forces of an incompressible fluid in an unbounded domain. Eq. (47) is solved with a FE-mesh with $N_x\times N_y$ elements and any fluid grid with $\mathcal{N}_x\times\mathcal{N}_y$ points.

4. Numerical results

In this section, the convergence of the proposed method is presented, and five geometries are investigated as numerical examples. The geometries are $l_p = 500\mu\mathrm{m}$ long, $h_p = 10\mu\mathrm{m}$ thick and the width w_p varies between $31.25\mu\mathrm{m}$ and $500\mu\mathrm{m}$. So the plate's aspect ratio r_a spans from 16 to 1, as shown in Fig. 7.

In the following numerical examples, the plates are comprised of isotropic silicon ($E_p = 169\mathrm{GPa}, \rho_p = 2330\mathrm{kg/m}^3, v_p = 0.3$). Here, silicon as isotropic material is used, so that a comparison with previous semi-analytic models for beams is possible. In the subSection 4.3.6, the material properties of silicon as an orthotropic material are defined. The fourth-order constitutive tensor $C_{\alpha\beta\gamma\delta}$ for an isotropic material is written from E_p and v_p as

$$C_{\alpha\beta\gamma\delta} = \left[\frac{E_p\left(\delta_{\alpha\gamma}\delta_{\beta\delta} + \delta_{\alpha\delta}\delta_{\beta\gamma}\right)}{2\left(1+v_p\right)} + \frac{E_p v_p}{1-v_p^2}\delta_{\alpha\beta}\delta_{\gamma\delta}\right]. \quad (48)$$

The plates are considered immersed in water at 25°C ($\rho_f = 997\mathrm{kg/m}^3, \mu_f = 0.89\mathrm{mPa\,s}$). For all following analyses, the degree of the function space $\mathcal{W}^h$ is 2. Any degree higher than or equal to two can be used [22].

4.1. Convergence

Three aspects of the convergence of the present method must be inspected: the IP method convergence, the Chebyshev-Gauss integration convergence, and the complete method convergence.
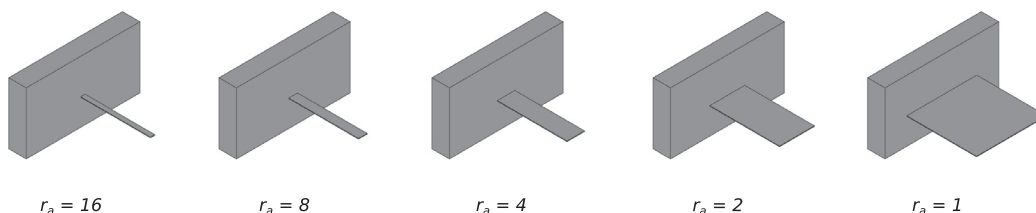

$r_a = 16$ $\qquad$ $r_a = 8$ $\qquad$ $r_a = 4$ $\qquad$ $r_a = 2$ $\qquad$ $r_a = 1$

Fig. 7. Geometries with aspect ratio r_a between 16 and 1 are analyzed as the numerical examples.

For the convergence analysis, we focus on the plate with $r_a = 4$ at three different representative frequencies: 10 kHz, 100 kHz, 1 MHz.

The FE meshes comprise r_a times as many elements in x-direction as there are in y-direction, $N_x = r_a N_y$. Using such meshes the internal angles between edges are equal, which minimizes the numerical error. In the convergence analyses a quasi-square fluid grid with $\mathcal{N}_y = \mathcal{N}_x - 1$ is considered.

4.1.1. IP method

To check the convergence of the IP method, the Kirchhoff plate equation without the fluid force term, i.e., Eq. (47) without the pressure difference, is considered. To quantify the convergence of the IP method, the L^2 norm of the difference between solutions $\hat{\phi}^i$ and $\hat{\phi}^{i-1}$ obtained with two consecutively refined FE-meshes is introduced as

$$||\epsilon^i||_{L^2} = \frac{||\hat{\phi}^i - \hat{\phi}^{i-1}||_{L^2}}{\max\left(||\hat{\phi}^i||_{L^2}, ||\hat{\phi}^{i-1}||_{L^2}\right)}. \tag{49}$$

Fig. 8 shows $||\epsilon||_{L^2}$ with the number of elements N_x at 10 kHz, 100 kHz and 1 MHz for penalty parameters τ between 8 and 64. For any $\tau \geq 8$, the IP method is convergent at all frequencies, while for $\tau < 8$, solutions diverge and are not shown. The exponent of the convergence according to the power-law (convergence rate) varies between 1.25 and 2 at different frequencies, and is not altered with different penalty parameters τ at the same frequency. These results

agree with the observation by Engel et al. [22] that the stabilization parameter τ is not critical for convergence if chosen large enough, and that the rate of convergence is independent of the value of τ.

The solution diverges for very fine meshes with $N_x > 128$ at low frequencies (10 kHz and 100 kHz) for all penalty parameters τ. This divergence is related to the IP method for Kirchhoff plates. The IP method imposes C1-continuity of the basis functions by penalising discontinuities in the derivatives of the basis functions. This penalisation exhibits instability at very fine meshes at low frequencies [22]. At higher frequencies, this instability occurs only with finer meshes than it does for low frequency. For instance, at 1 MHz $||\epsilon||_{L^2}$ is convergent up to $N_x = 256$, while at lower frequencies it diverges at $N_x \geq 256$. Also note that at 1 MHz the mesh with $N_x \leq 32$ is too coarse to describe a high-order vibrational mode of the plate, which causes $||\epsilon||_{L^2}$ to be in the order of 1 and non-convergent until a mesh with $N_x = 32$ is used.

In the following investigations, the FE-meshes are refined to a maximum of $N_x = 128$ elements, as they are the finest FE-mesh with convergent behavior at any given frequency. Concerning the value of the penalty parameter τ, the IP method is convergent for $\tau >= 8$. In the following analyses, τ is set to 16 to ensure with a safety margin that the method operates in the convergence regime.

4.1.2. Chebyshev-Gauss convergence

In order for the proposed method to be convergent, integration of the pressure difference $\Delta\hat{p}$ with Chebyshev-Gauss quadrature as written in Eq. (46) has to be convergent. To examine the convergence of the Chebyshev-Gauss numerical integration, a matrix **P** is defined, whose elements P_{ij} are
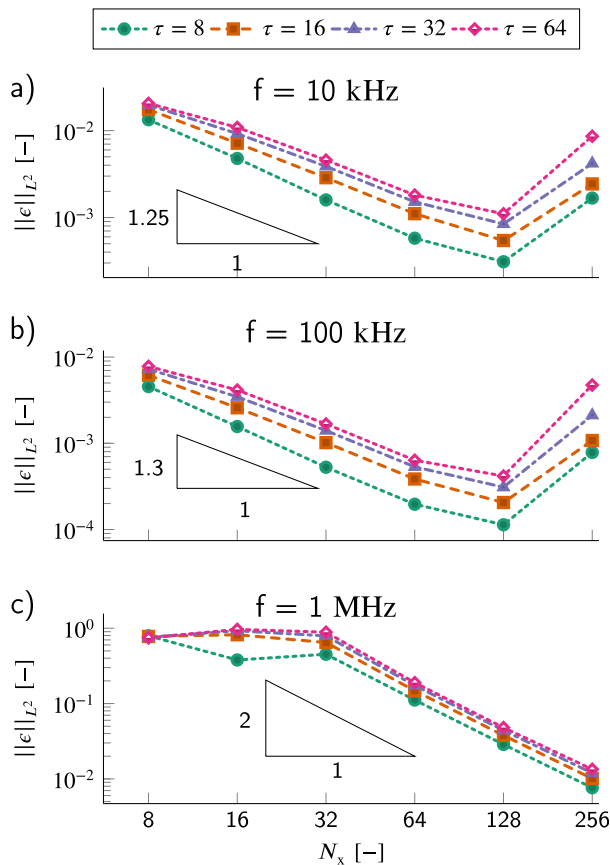

Fig. 8. Convergence of IP method for the plate $r_a = 4$ as a function of the number of elements N_x in the FE-mesh for penalty parameters τ between 8 and 64 at (a) 10 kHz, (b) 100 kHz and (c) 1 MHz.
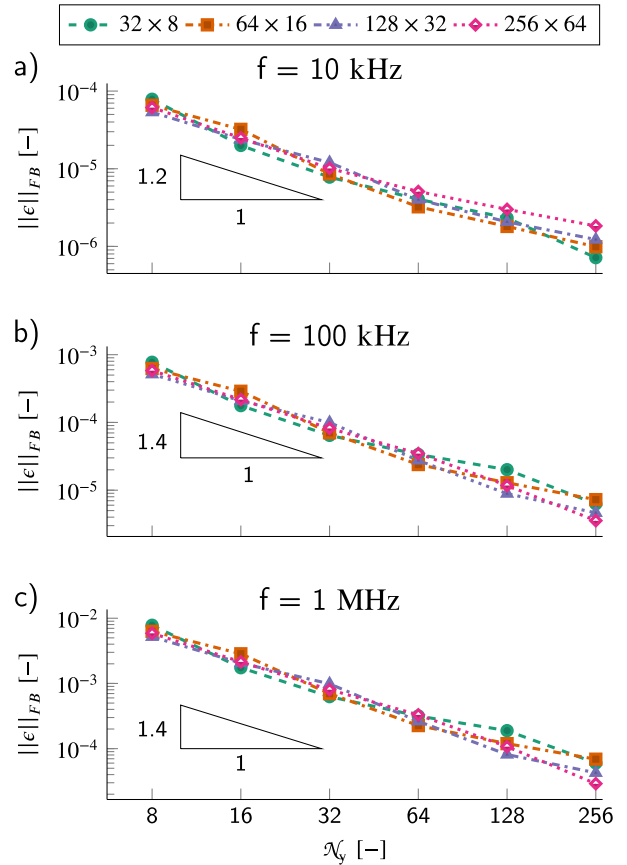

Fig. 9. Convergence of the Chebyshev-Gauss quadrature integration of the plate with $r_a = 4$ as a function of the number of fluid grid points $\mathcal{N}_y$ for different FE-meshes ($N_x \times N_y$) at (a) 10 kHz, (b) 100 kHz and (c) 1 MHz.

$$P_{ij} = \frac{\pi}{\mathcal{N}_y} \mu_f j\omega \sum_{k=1}^{\mathcal{N}_x} \varpi_k \sum_{l=1}^{\mathcal{N}_y} \sum_{m=1}^{\mathcal{N}_y} A_{lm}^{-1} \psi_i^h(x_k, y_l)$$
$$\psi_j^h(x_k, y_m) \sqrt{(w_p/2)^2 - y_j^2}, \quad (50)$$

where ψ_i^h is the i-th basis function of W^h. The matrix **P** is a projection of the pressure difference $\Delta\hat{p}$ generated at the j-th basis function on the i-th basis function. To quantify the convergence of **P**, the Frobenius norm of **P** is introduced as

$$||\epsilon^i||_{FB} = \frac{||\mathbf{P}^i - \mathbf{P}^{i-1}||_{FB}}{\max\left(||\mathbf{P}^i||_{FB}, ||\mathbf{P}^{i-1}||_{FB}\right)}, \quad (51)$$

where $\mathbf{P}^i$ and $\mathbf{P}^{i-1}$ are pressure matrices obtained with consecutively refined fluid grids for a similar FE-mesh. Four different FE-meshes $N_x \times N_y$ are used, they are $32 \times 8, 64 \times 16, 128 \times 32$ and 256×64.

Fig. 9 shows $||\epsilon||_{FB}$ as a function of the fluid grid points $\mathcal{N}_y$. The fluid grid $\mathcal{N}_x \times \mathcal{N}_y$ ranges from 9×8 to 257×256 grid points. At all frequencies and for all FE-mesh, the integration converges with a convergence rate that varies between 1.2 and 1.4. Hence, the Chebyshev-Gauss integration of $\Delta\hat{p}$ as defined by Eq. (46) is stable and convergent.

4.1.3. Complete method convergence

The convergence of the solutions obtained with the complete proposed method as described by Eq. (47) is here inspected. Quasi-square fluid grids of $33 \times 32, 65 \times 64, 129 \times 128$, and 257×256 are employed for this analysis.

Fig. 10 shows $||\epsilon||_{L_2}$ at 10 kHz, 100 kHz and 1 MHz with the number of FE-mesh elements in x-direction N_x. At 10 kHz, the proposed method converges with a convergence rate equals 1.25 for a FE-mesh discretized up to $N_x = 128$ elements. For $N_x > 128$, solution $\hat{\phi}$ diverges, similarly to the IP method convergence results at 10 kHz in Fig. 8. Thus at 10 kHz the convergence/divergence behavior of the complete method is dominated by the convergence/divergence of the IP method. At 100 kHz and 1 MHz, the method converges with rate equals to 1.7 and 2, respectively. Interestingly, the complete method does not diverge at 100 kHz for $N_x \geqslant 256$ as it occurs in the IP method convergence analysis. This means that at 100 kHz the convergence of the method is dominated by the Chebyshev-Gauss convergence.

From the convergence results shown in this section, $\tau = 16$ and $N_x \leqslant 128$ are defined as parameters to be used in the following investigations, since they provide convergence at the three representative frequencies for any fluid grid.

4.2. Slender plates

In the following subsections we analyze the slender plates with $r_a = 16, 8,$ and 4. Results obtained with the present method are compared with the ones obtained with the semi-analytic models for flexural modes (Sader [57]) and for torsional modes (Green [31]).

4.2.1. Displacement spectrum

Fig. 11 shows the absolute displacement spectrum $|\hat{\phi}_c|$ of the slender plates at their free corner at $x = l_p$, $y = w_p/2$ due to an uni-
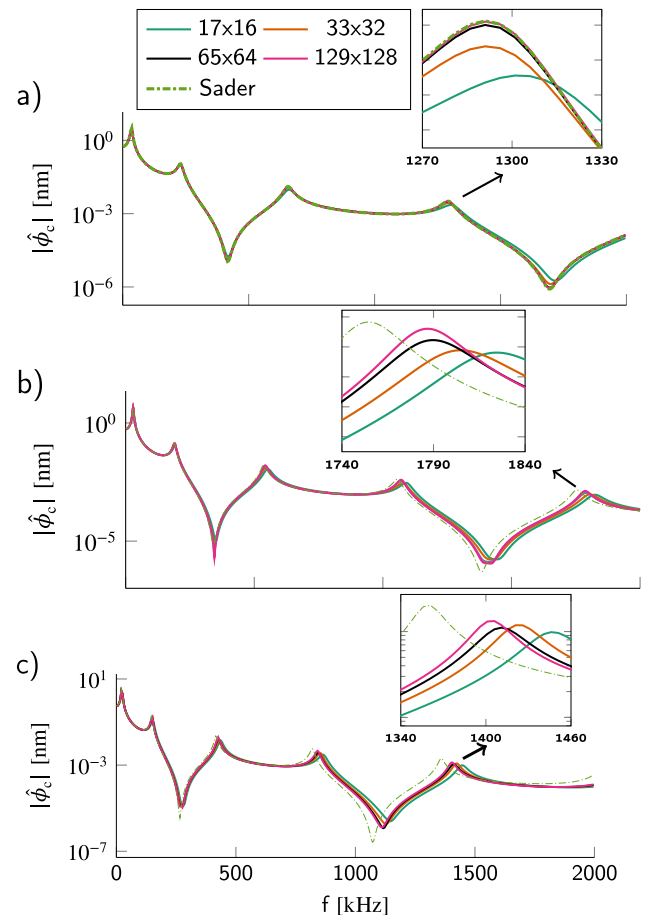

Fig. 10. Convergence of the L^2 norm of the displacement $||\epsilon||_{l^2}$ as a function of the number of elements N_x in the FE-mesh of the plate with $r_a = 4$ using different fluid grids ($\mathcal{N}_x \times \mathcal{N}_y$) at (a) 10 kHz, (b) 100 kHz and (c) 1 MHz.

Fig. 11. Absolute displacement spectrum $|\hat{\phi}_c|$ of the slender plates with aspects ratios a) $r_a = 16$, b) $r_a = 8$ and c) $r_a = 4$ for different fluid grids $\mathcal{N}_x \times \mathcal{N}_y$.

form load $\hat{q} = 1$Pa. The free corner is chosen because it is not on or close to a nodal line of any vibrational modes. The considered frequency band ranges from 1 kHz to 2 MHz with 1 kHz discretization. Quasi-square fluid grids $\mathcal{N}_y = \mathcal{N}_x - 1$ are used, because they converge quicker than rectangular grids related by the aspect ratio $\mathcal{N}_y = (\mathcal{N}_x - 1)/r_a$. This is discussed in detail in A.

For the slender plate with $r_a = 16$, $|\hat{\phi}_c|$ converges exactly to Sader's solution as the fluid grid is refined to 129×128 points as shown in Fig. 11a. This is an important result, as it shows that the proposed method is consistent with the semi-analytic model for flexural modes of beams in viscous fluids. For the plates with smaller aspect ratio $r_a = 8$ and $r_a = 4$, $|\hat{\phi}_c|$ obtained with the present method does not match exactly Sader's solution. This differences occur because, for the lower aspect ratio plates ($r_a = 8$ and $r_a = 4$), the structure's dynamics is less well approximated by a one-dimensional beam model, and the lateral strain components must be considered. Therefore to predict the flexural modes of plates with $r_a \leqslant 8$, the present method provides more accurate results than models based on the Euler–Bernoulli equation.

4.2.2. Quality factor

The quality factor of each vibrational mode is obtained from the absolute displacement spectrum. To evaluate Q, we fit the spectral response function of the damped simple harmonic oscillator (SHO)

$$\phi_{\text{sho}}(f) = \frac{a}{f^2 - f_d^2 + \mathrm{j} f f_d / Q} + b, \tag{52}$$

to each damped resonance frequency f_d. In Eq. (52), a and b are amplitude and offset fitting parameters, respectively. This definition of Q based on the SHO equation renders similar results to the Q-factor definition based on dissipated energy in Eq. (1).

Convergence of Q and f_d with the fluid grid is discussed in B for the three slender geometries. The Q-factor is considered converged when the difference between the Q-factors obtained with two consecutively refined fluid grids is smaller than 1%. For resonance frequency convergence, the difference must be smaller than 0.1%. Higher-order flexural modes (higher n_x) require finer fluid grids for convergence of Q and f_d. And, the wider the structures (higher r_a), the finer the fluid grid required for convergence Q and f_d.

Fig. 12 shows the converged quality factors of the flexural and torsional modes. In addition to the present method's prediction, Q obtained with Sader's method [57] for flexural modes and with Green's method [31] for torsional modes are shown. For the slender plate with $r_a = 16$, the quality factors Q of flexural modes agree within 0.1% to those obtained with Sader's method. For the (1,1) torsional mode, a Q which differs by 2% from Green's prediction is obtained. As r_a decreases to $r_a = 8$ and $r_a = 4$, the quality factor differences to Sader's and Green's models increase. For the plate with $r_a = 4$, this difference reaches 4% for the (5,0) mode compared to Sader's model, and 10% for the (3,1) mode in comparison to Green's model. Besides the difference in Q-factors, there is a significant difference in the damped resonance frequencies between the present method and the one-dimensional models, especially with Green's method for torsional modes. For the (3,1) mode, for instance, there is a 17% difference in f_d prediction.

4.2.3. Added-mass effect

In addition to the Q-factor, for MEMS resonators it is essential to quantify the added mass effect caused by the fluid. This is achieved with the fluid-added-mass-per-plate-mass-ratio $\mathcal{M}$, defined as

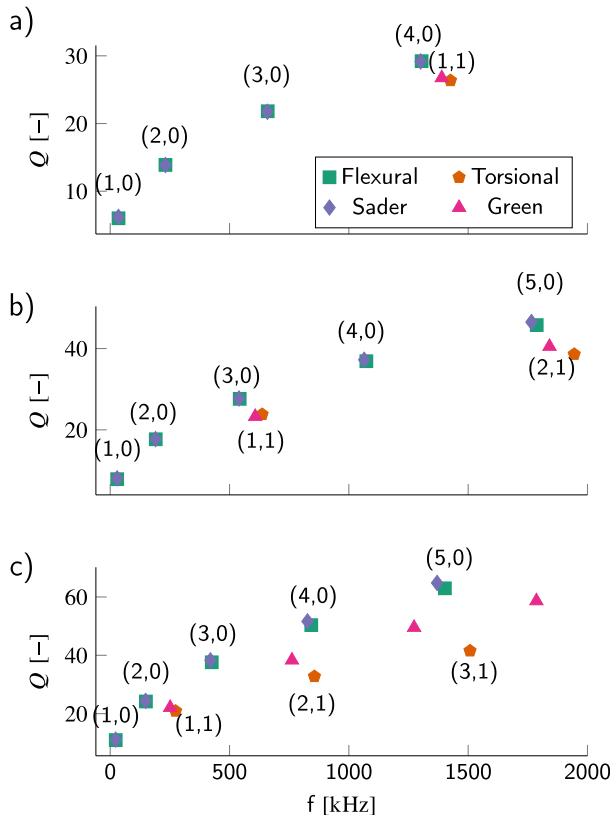$$\mathcal{M} = \frac{m_{\text{added}}}{m_{\text{plate}}} = \frac{f_n^2}{f_d^2} - 1. \tag{53}$$

Fig. 12. Quality factor of the vibrational modes of the plates with a) $r_a = 16$, b) $r_a = 8$ and c) $r_a = 4$.
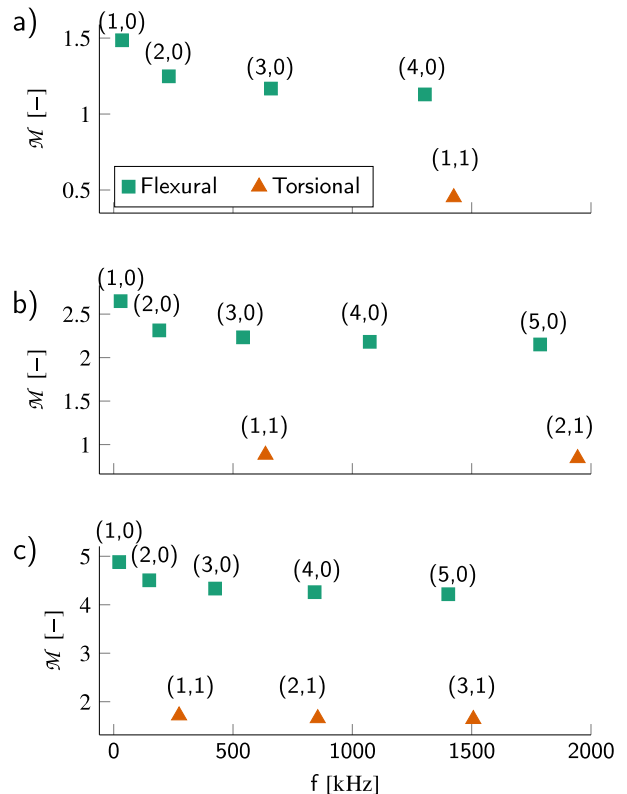

Fig. 13. Fluid-added-mass-per-plate-mass-ratio $\mathcal{M}$ of the plates with a) $r_a = 16$, b) $r_a = 8$ and c) $r_a = 4$.

$\mathcal{M}$ quantifies the added mass effect, characterized by the reduction of the resonance frequency of a resonator in vacuum f_n to its damped resonance frequency in a fluid f_d [5]. When $f_d \approx f_n$ the added mass is negligible and $\mathcal{M} \approx 0$.

Fig. 13 shows $\mathcal{M}$ of the slender plates up to 2 MHz. The flexural modes exhibit much higher $\mathcal{M}$ than the torsional modes for the three structures. $\mathcal{M}$ increases with the width of the plate for flexural and torsional modes, which means that wider plates exhibit larger reduction in f_n to f_d than slender beams.

4.3. Rectangular plate with r = 2

The proposed method is, of course, not limited to slender beam structures, and its purpose is exactly the simulation of wider structures. To demonstrate the method's capabilities, a plate with $r_a = 2$ (Fig. 7) in water is considered as an example for which the displacement spectrum, mode shapes, pressure difference, quality factors, and fluid-added-mass-per-plate-mass-ratio $\mathcal{M}$ are not predictable with existing semi-analytical methods. A point force of amplitude $\widehat{F} = w_p \times l_p \times \hat{q}$ excites the plate at its free corner $x = l_p$ and $y = w_p/2$. $\widehat{F}$ is applied at the plate's free corner so that all vibrational modes are excited.
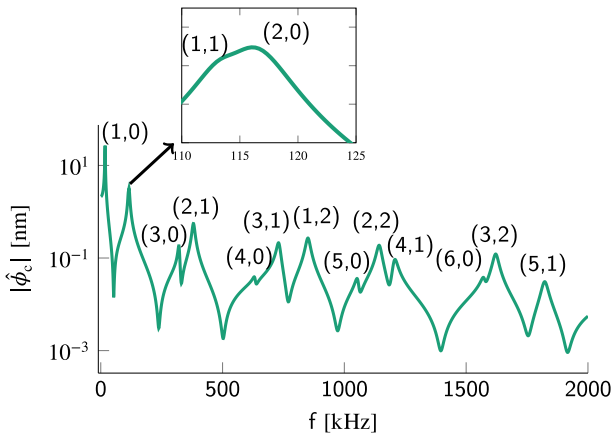
Fig. 14. Absolute displacement spectrum $|\hat{\phi}_c|$ of the plate with $r_a = 2$ obtained with 128×64 FE-mesh and 129×128 fluid grid. Peaks correspond to the vibrational modes characterized by (n_x, n_y).

4.3.1. Displacement spectrum

Fig. 14 shows the absolute displacement spectrum of the plate's corner $|\hat{\phi}_c|$ obtained with a 129×128 fluid grid. Note in Fig. 14, that there are several additional resonance peaks present in the same frequency range of 2 MHz in comparison to the slender plates shown in Fig. 11. Resonance peaks in $|\hat{\phi}_c|$ correspond to flexural $(n_x, 0)$, torsional $(n_x, 1)$, roof tile-shaped $(1, n_y \geqslant 2)$ or other non-conventional (neither torsional, nor flexural nor roof-tile shaped) plate modes $(n_x \geqslant 2, n_y \geqslant 2)$.

4.3.2. Vibrational modes

The absolute displacement $|\hat{\phi}|$ of the 6 flexural vibrational modes of the plate $r_a = 2$ up to 2 MHz are shown in Fig. 15. The displacement $|\hat{\phi}|$ at the second flexural mode (2,0) in Fig. 15b is dominated by the torsional mode (1,1), which is shown in Fig. 16a. This modal overlap occurs because the resonance frequency f_d of the flexural mode (2,0) is very close to f_d of the torsional mode (1,1). With the point force $\widehat{F}$ at the plate's corner, the torsional mode (1,1) is more strongly excited than the flexural mode (2,0). This phenomenon can not be predicted by other semi-analytic methods, as they only predict either the flexural modes or the torsional modes of these structures separately.

The additional 8 peaks in Fig. 14 refer to the torsional $(n_x, 1)$, the first roof tile-shaped (1,2) and non-conventional $(n_x \geqslant 2, n_y \geqslant 2)$ vibrational modes, which are shown in Fig. 16. Note that the dynamics of the roof tile-shaped and non-conventional vibrational modes can be predicted only with the proposed method or with purely numerical methods, but not with semi-analytic models.

4.3.3. Pressure difference

With the proposed method, it is possible to further understand the pressure with which the fluid acts on the plates vibrating at different modes. The pressure difference $\Delta \hat{\mathbf{p}}$ is calculated at a cross-section of the plate with Eq. (40). The plate's tip $x = l_p$ is a suitable choice as a position where no nodal lines in y-direction occur, i.e. where $\hat{\phi}$ is non-zero. Fig. 17 shows the imaginary component of the pressure difference at the flexural (1,0), torsional (1,1), and roof tile-shaped (1,2) vibrational modes of the rectangular plate. The number of grid points $\mathcal{N}_y$ varies from $\mathcal{N}_y = 16$ to $\mathcal{N}_y = 256$. For the three modes, the inverse square root singularity of $\Delta \hat{\mathbf{p}}$ towards the edges $y = 125\mu m$ is present. What is more, from Fig. 17, it is clear, at least $\mathcal{N}_y \geqslant 256$ is required so that the inverse square root singularity towards the edge is well represented.

(a) Mode (1,0).   (b) Mode (2,0)*.   (c) Mode (3,0).

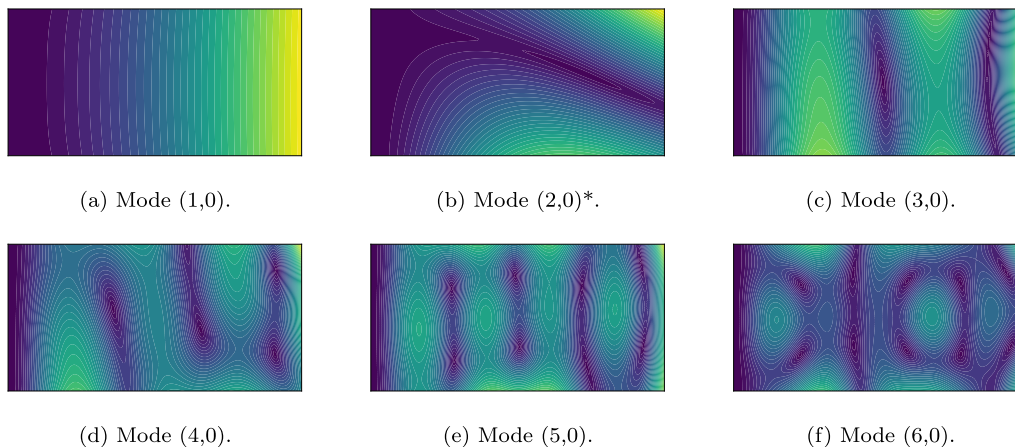
(d) Mode (4,0).   (e) Mode (5,0).   (f) Mode (6,0).

Fig. 15. Absolute displacement of the flexural modes $(n_x, 0)$ of the plate $r_a = 2$. The flexural mode (2,0)* is dominated by the torsional mode (1,1). The absolute displacement is normalized between 0 (blue) and 1 (yellow).

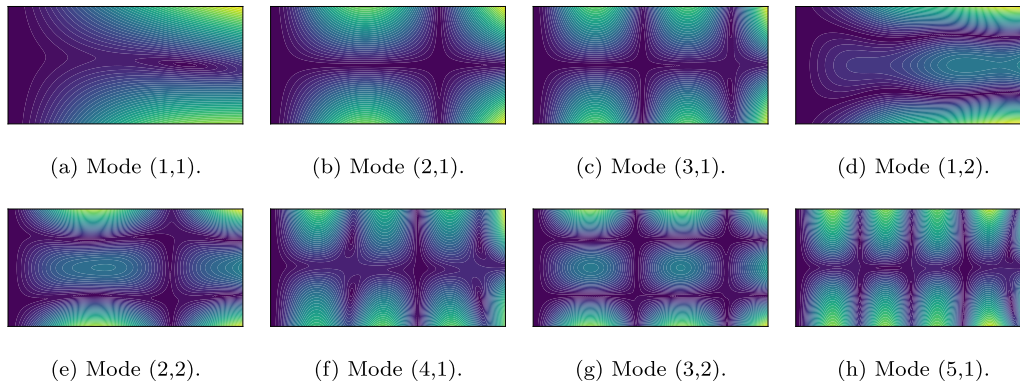(a) Mode (1,1).   (b) Mode (2,1).   (c) Mode (3,1).   (d) Mode (1,2).

(e) Mode (2,2).   (f) Mode (4,1).   (g) Mode (3,2).   (h) Mode (5,1).

Fig. 16. Absolute displacement of the torsional $(n_x,1)$, roof tile-shaped $(1,2)$ and other non-conventional $(n_x \geqslant 2, n_y \geqslant 2)$ vibrational modes of the plate $r_a = 2$. The absolute displacement is normalized between 0 (blue) and 1 (yellow). (For interpretation of the references to colour in this figure legend, the reader is referred to the web version of this article.)
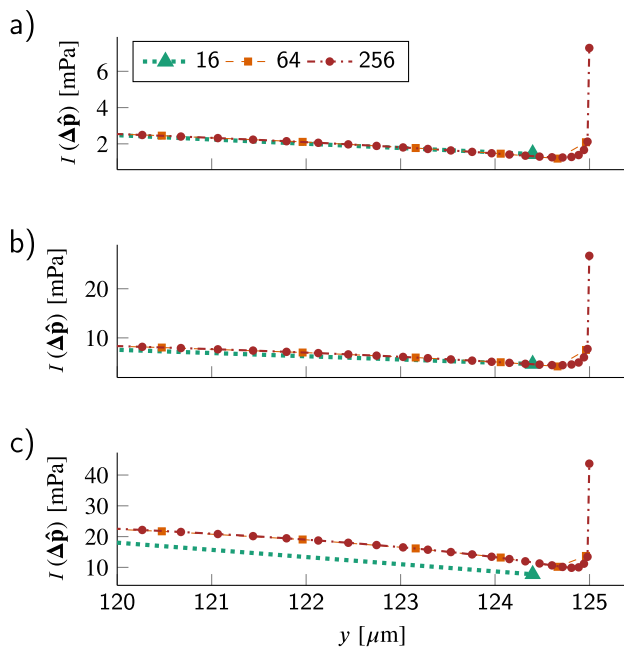
Fig. 17. Imaginary pressure difference at the free edge $x = l_p$ at a) the first flexural mode $(1,0)$ and b) the torsional mode $(1,1)$ and c) the roof tile-shaped mode $(1,2)$ with different number of fluid grids points $\mathcal{N}_y$. The edge of the plate is at $y = 125\,\mu m$.

Fig. 18. Quality factor Q of the plate with $r_a = 2$ arranged according to its vibrational mode in flexural, torsional, roof tile-shaped, and non-conventional vibrational modes.

Fig. 19. Fluid-added-mass-per-plate-mass-ratio $\mathcal{M}$ of the plate with $r_a = 2$ arranged according to its vibrational mode.

4.3.4. Quality factor

Fig. 18 shows the Q-factors of the vibrational modes of the rectangular plate $r_a = 2$ categorized in flexural, torsional, roof tile, and non-conventional modes. The Q-factors shown in Fig. 18 converged with less than 1% variation for a fluid grid of 2049×2048 points, as shown in B. In this frequency range, Q of the flexural modes are the highest, reaching a value of 130 for the $(6,0)$ mode. Note that the Q-factor of the roof tile-shaped $(1,2)$ mode is much higher than the Q of the first flexural mode $(1,0)$, but not higher than higher-order flexural modes as the $(4,0)$ mode which have close damped resonance frequencies.

4.3.5. Added mass effect

Fig. 19 shows the fluid-added-mass-per-plate-mass-ratio $\mathcal{M}$ of the rectangular plate up to 2 MHz. The roof tile-shaped mode and the non-conventional modes exhibit lower $\mathcal{M}$ than the tor-

sional modes, which in turn have lower $\mathcal{M}$ than flexural modes. Hence for the rectangular plate in water, the higher the number of nodal lines n_y, the smaller the added-mass effect.

4.3.6. Orthotropic material

Silicon is an orthotropic material, whose elastic tensor $c_{\alpha\beta\gamma\delta}$ has 8 non-zero entries [61]. For a standard (100) silicon wafer the elas-
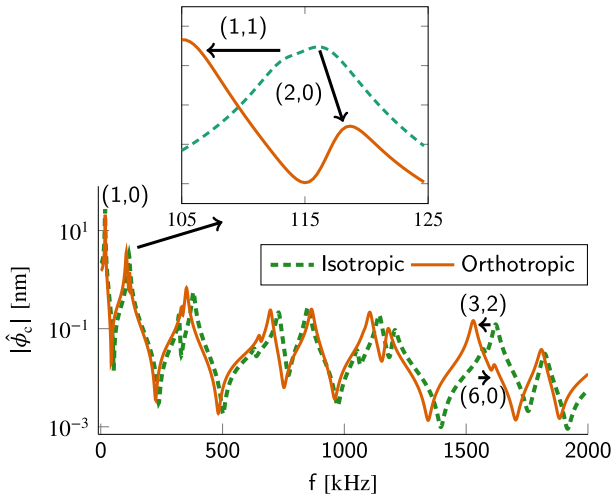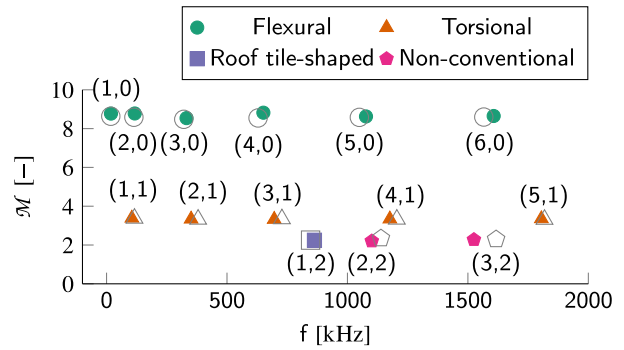
Fig. 20. Absolute displacement spectrum $|\hat{\phi}_c|$ of the plate with $r_a = 2$ obtained with 128×64 FE-mesh and 129×128 fluid grid with isotropic and orthotropic materials.
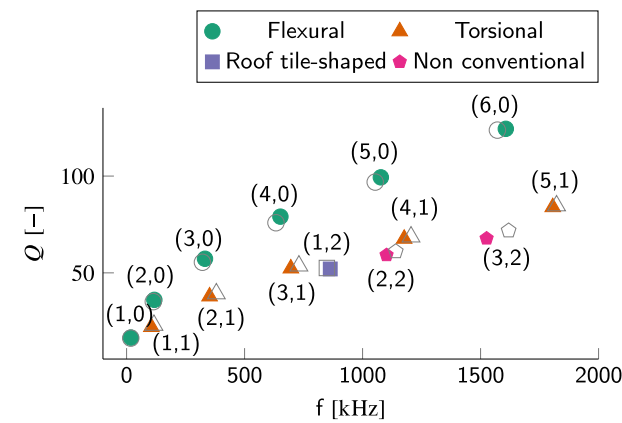

Fig. 21. Quality factor Q of the plate with $r_a = 2$ arranged according to its vibrational mode. Results for orthotropic silicon are shown in color, and for isotropic silicon in gray. (For interpretation of the references to colour in this figure legend, the reader is referred to the web version of this article.)

ticity constants are $C_{xxxx} = C_{yyyy} = 194.5$ GPa, $C_{xxyy} = C_{yyxx} = 35.7$ GPa, and $C_{xyxy} = C_{xyyx} = C_{yxyx} = C_{yxxy} = 50.9$ GPa [34].

Fig. 20 shows the spectral displacement of the plate with $r_a = 2$ considering silicon as isotropic and orthotropic materials. Considering silicon as an orthotropic material, slightly shifted resonance frequencies are obtained in comparison to the ones considering isotropic material. For instance, the peaks of the modes (2,0) and (1,1) with the isotropic model are very close in frequency, while with the orthotropic model they are clearly distinguishable. The damped resonance frequency of the (3,2) mode reduces from 1619 kHz with the isotropic model to 1525 kHz with the orthotropic model. And f_d of the (6,0) mode increases from 1571 kHz to 1620 kHz, when altering from isotropic to orthotropic models.

The Q-factor of the vibrational modes obtained with isotropic and orthotropic materials do not significantly differ from each other, as shown in Fig. 21. The Q-factors obtained for orthotropic material are displayed in color, and for isotropic material in gray. In Fig. 21 see that the damped resonance frequencies f_d of the flexural modes are lower with the isotropic model than with the orthotropic model. In contrast, f_d of the torsional modes are higher with the isotropic model.
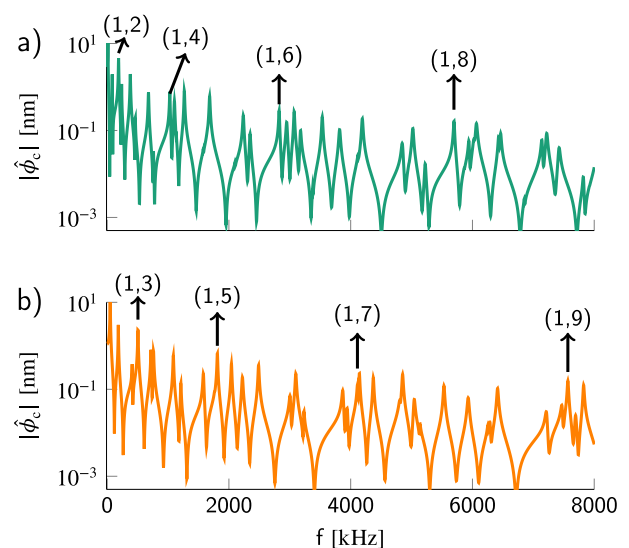

Fig. 22. Fluid-added-mass-per-plate-mass-ratio $\mathcal{M}$ of the plate with $r_a = 2$ arranged according to the vibrational modes. Results for orthotropic silicon are shown in color, and for isotropic silicon in gray.

Even though f_d changes with the material model, the fluid-added-mass-per-plate-mass-ratio $\mathcal{M}$ is not significantly altered with the inclusion of the direction dependent material properties of silicon, as shown in Fig. 22.

4.4. Square plate

As an interesting application example, the quality factors of a square micro-plate ($r_a = 1$) vibrating in the roof tile-shaped shaped vibrational modes are evaluated. Differently than for the rectangular plate $r_a = 2$, here two point forces at the two free corners of the plate at $x = l_p$ and $y = \pm w_p/2$ are considered. When the point forces are in phase, they are named symmetric excitation. When they are out-of-phase, they are referred to as asymmetric excitation. These excitations are employed so that the roof tile-shaped modes are more easily identified, due to the sheer amount of vibrational modes in the 8 MHz frequency range. A 128×128 FE-mesh with a 257×256 fluid grid is used to determine the plate's displacement spectrum which is shown in Fig. 23a and b with symmetric and asymmetric excitation, respectively. Up to the (1,9) roof tile-shaped mode in the 8 MHz frequency range is identified. Note that the flexural wavelength of the (1,9) roof tile-shaped mode is $\lambda_{1:9} = 125$ μm. The resonance frequency of this mode is

Fig. 23. Absolute displacement spectrum $|\hat{\phi}_c|$ of the plate with $r_a = 1$ with a) symmetric and b) asymmetric excitation.

(a) Mode (1,2). (b) Mode (1,3). (c) Mode (1,4). (d) Mode (1,5).

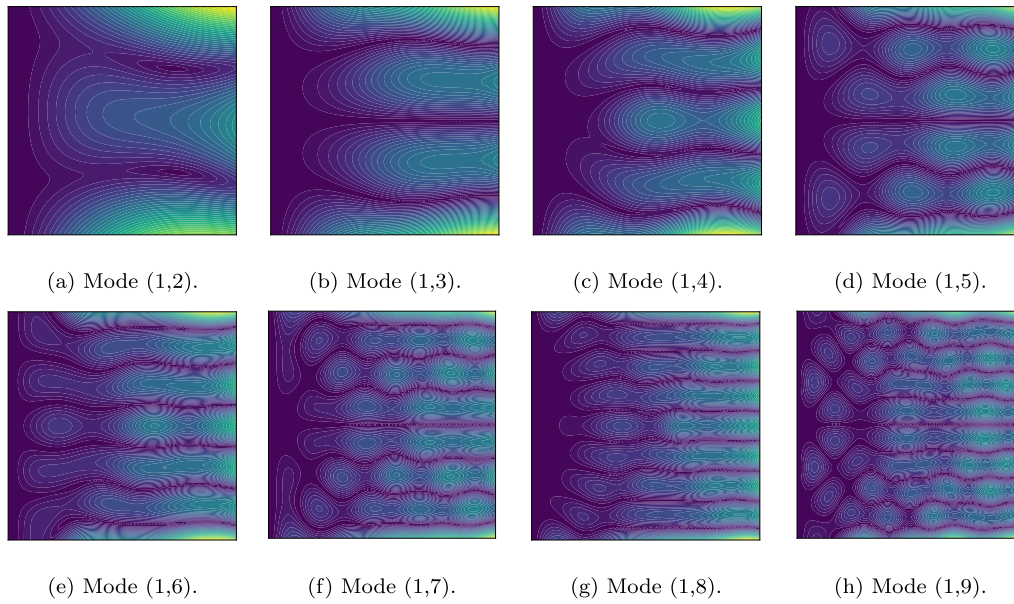(e) Mode (1,6). (f) Mode (1,7). (g) Mode (1,8). (h) Mode (1,9).

Fig. 24. Absolute displacement $|\hat{\phi}|$ of the roof tile-shaped vibrational modes of the plate with aspect ratio $r_a = 1$. The absolute displacement is normalized between 0 (blue) and 1 (yellow).
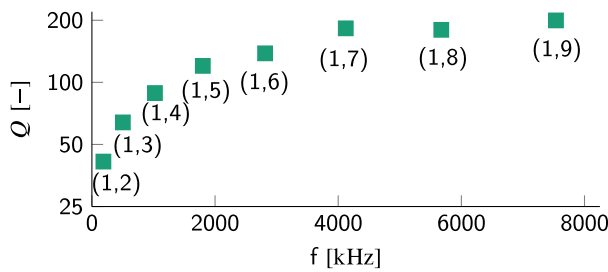

Fig. 25. Q-factor of the roof tile-shaped modes of the plate with $r_a = 1$ in the 8 MHz frequency range.

Fig. 26. Q-factor Q and fluid-added-mass-per-plate-mass-ratio $\mathcal{M}$ of flexural modes of a slender plate predicted by a purely numerical method [5] and with the. present method.

7.52 MHz, which means that the acoustic wavelength is $\lambda_{ac} = 199$ μm. Thus even at this high frequency, water flow around the micro-plate is incompressible.

Fig. 24 shows the absolute displacement $|\hat{\phi}|$ of the roof tile-shaped vibrational modes, from the (1,2) up to the (1,9).

The Q-factor associated with each roof tile-shaped mode in the 8 MHz frequency range is shown in Fig. 25. Q-factors shown in 25 converged with less than 1% variation with fluid grid equals 8193 × 8192. The roof tile-shaped vibrational modes exhibit an increasing Q, reaching values as high as 200 for the (1,9) mode. This high Q-factor pattern is consistent with experimentally obtained quality factors of micro-plates in liquids [39,56,48].

4.5. Numerical comparison

An important assumption in the present method is the two-dimensional fluid flow approximation, as discussed in detail in Section 3.2. Here the Q-factor and $\mathcal{M}$ calculated with the present method and with a purely numerical method and reported by Basak et al. [5] are compared. The silicon micro-plate has length equals 197 μm, width equals 29 μm ($r_a \approx 6.5$), and the thickness is 2μm.

The Q-factor and $\mathcal{M}$ of the first six flexural modes of this slender plate in water are shown in Fig. 26. Q-factor with the purely
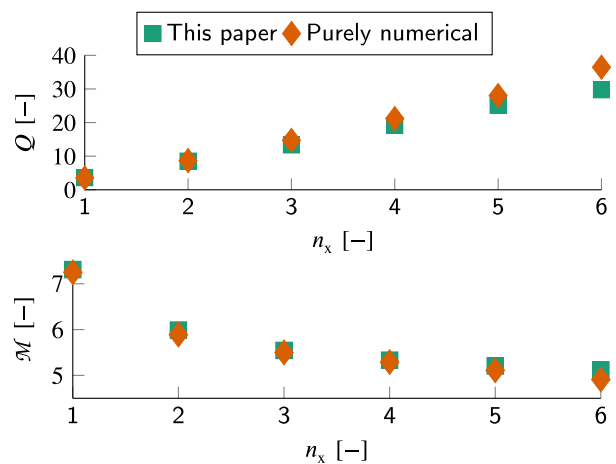
numerical method agree with the present method's prediction within 10% for the low order modes ($n_x \leqslant 4$). For higher n_x, the difference in Q-factors increases, reaching 20% difference for the (6,0) mode. There are minimal differences in $\mathcal{M}$ (smaller than 5%) with the two methods up to the sixth flexural mode. Results shown in Fig. 26 agree with previous findings of studies that used purely numerical methods [5,7,24,42] that the two-dimensional fluid flow approximation results in an underestimated resonance frequency, which in turns yields an overestimated added mass, as well as under-estimated Q-factor.

4.6. Experimental comparison

To validate the proposed semi-numerical method we resort to published experimental data on the Q-factor of micro-plates in a viscous fluids. Here a silicon micro-plate which is 500μm long, 300 μm wide ($r_a \approx 1.66$) and 11.5 μm thick is investigated [55].
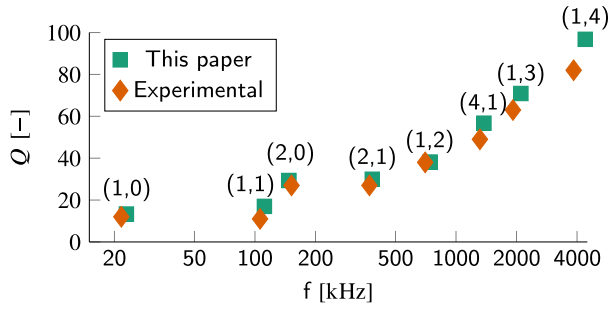
Fig. 27. Quality factor Q of different vibrational modes of a wide micro-plate in isopropanol.

Fig. 28. Fluid-added-mass-per-plate-mass-ratio $\mathcal{M}$ of roof tile-shaped modes of a rectangular micro-plate in isopropanol.

The fluid used in the experiments is isopropanol with $\mu_f = 2.1062 \text{mPa s}$ and density $\rho_f = 781.2 \text{kg/m}^3$. Silicon is here considered as an orthotropic material with similar material tensor as described in Section 4.3.6.

Fig. 27 shows the Q-factor of the reported vibrational modes obtained experimentally and calculated with the present method. Results include not only roof tile-shaped modes, but also other low order modes [55]. Excellent agreement between simulated and experimental Q-factors is found. Notably, we observe exceptional agreement with all vibrational modes up to the (1,2) mode at 750 kHz. For the three higher frequency vibrational modes, the prediction and experimental Q-factors differ by less than 10%[7], which is a smaller difference than the errors reported using purely numerical methods [5,7].

Additional studies focused exclusively on the roof tile-shaped modes, for example a micro-plate with $l_p = 2524 \mu\text{m}, w_p = 1274$ μm ($r_a \approx 2$), and $h_p = 22$ μm in isopropanol [48,55]. The experimental fluid-added-mass-per-plate-mass-ratio $\mathcal{M}$ of the roof tile-shaped modes up to 2 MHz are shown in Fig. 28. The present method slightly over-predicts $\mathcal{M}$ for all roof tile-shaped modes by $15 \pm 2\%$, while the damped resonance frequencies show very good agreement.

The Q-factors of the roof tile-shaped modes of the same plate are shown in Fig. 29. Excellent agreement between the present method's prediction and experimental data is found. Predicted Q-factors are within the experimental errors for most of the evaluated modes, being the only exceptions the (1,4) and (1,5) modes, for which the present method under-predicts the Q-factors by 10%[8]. Fig. 29 shows also the Q-factor obtained with a purely numerical method from Ruiz Diez et al. [55]. With the purely numerical method, good agreement in Q-factor is found only for the (1,2) mode. For the (1,3) mode, Q is over-predicted, whereas for the higher order roof tile-shaped modes (1,4) to (1,8) Q is under-predicted. For instance, the Q-factor of the (1,8) mode is under-estimated by 50.2% with the purely numerical method. Moreover, the purely numerical method under-predicts the resonance frequencies of all roof tile-shaped modes. Results in Fig. 29 evidence that the proposed method surpasses the accuracy of purely numerical methods in the estimation of both resonance frequencies and Q-factors of micro-plates in viscous fluids.

Fig. 29. Q-factor of the roof tile-shaped modes of a rectangular micro-plate in isopropanol. Experimental and purely numerical results are obtained from Ruiz Diez et al. [55].

5. Conclusions

This work describes a semi-numerical method to determine the dynamics of micro-plates immersed in incompressible viscous fluids. The proposed method goes beyond the semi-analytical models by accounting for two-dimensional vibrational modes of plates rather than simply one-dimensional modes of beams. The present model is especially valid and accurate for micro-plates in liquids and gases in ambient and low-pressure conditions.

The method converges at all frequencies with a convergence rate between 1.25 and 2. Numerical results for the slender plates with aspect ratios $r_a = 16, r_a = 8$ and $r_a = 4$ show that the proposed method properly generalizes previous semi-analytical methods for slender structures. What is more, the proposed method can show the limits of semi-analytic models for flexural and torsional modes of slender structures. For a plate with $r_a = 4$, the difference in Q-factor prediction between the proposed method and semi-analytical models [57,31] reach 4% and 10% for flexural and torsional modes, respectively.

As an application example, we investigate the dynamics of a rectangular plate with $r_a = 2$ for which displacement spectrum, mode shapes, pressure difference, quality factors, and fluid-added-mass-per-plate-mass-ratio $\mathcal{M}$ are not predictable with existing models. With the analysis of a square-sized plate with $r_a = 1$, the capabilities of the present method to investigate micro-plates vibrating at roof tile-shaped modes is displayed.

Comparison to purely numerical results shows that the two-dimensional fluid flow assumption in the proposed method yields Q-factors prediction within 20% up to the (6,0) mode. What is more, excellent agreement to experimental data of micro-plates in liquids (Figs. 27–29) is found. These results ensure that the presented method accurately predicts the Q-factor and the fluid-added-mass-per-plate-mass-ratio $\mathcal{M}$ of micro-plates in viscous fluids, even to a higher accuracy than purely numerical methods.

---

[7] Compressibility is not the reason for this 10% difference, since even for the (1,4) mode at 4.12 MHz the acoustic wavelength (276 μm) is larger than the flexural wavelength of the (1,4) mode (151 μm).

[8] Note that isopropanol is incompressible even for the (1,8) mode, because the acoustic wavelength at 1.92 MHz is 592 μm, which is much larger than the flexural wavelength of the (1,8) mode that is 320 μm The acoustic wavelength is calculated considering the speed of sound of isopropanol as 1139 m s^{-1} [55]. The flexural wavelength is calculated using a two-dimensional Fourier transform.
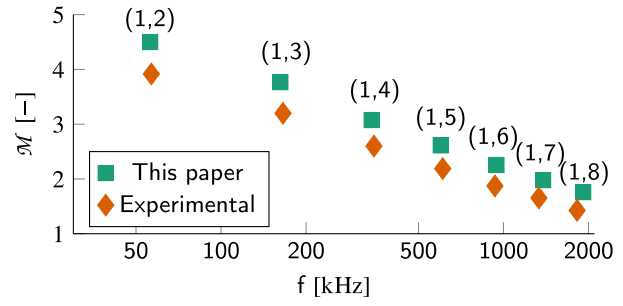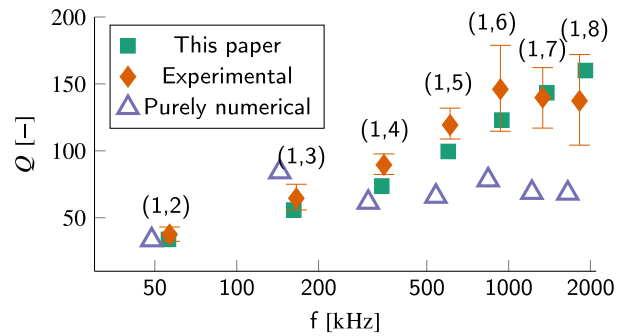
The numerical examples and comparisons to published data highlight that a semi-numerical method for predicting the non-conventional (neither torsional nor flexural) vibrational modes of MEMS micro-plates in viscous fluids has been missing. We anticipate that the proposed method will enable the investigation of MEMS resonator geometries utilizing non-conventional vibrational modes of plates, thus inspiring novel device architectures to perform with unprecedentedly high quality-factors in viscous fluids.

Author contributions

Ulrich Schmid started the research. Andre Gesing and Daniel Platz developed the mathematical formulation. Andre Gesing performed the simulations, analyzed the data, and wrote the manuscript. All authors contributed to the discussion of the results.

Declaration of Competing Interest

The authors declare that they have no known competing financial interests or personal relationships that could have appeared to influence the work reported in this paper.

Acknowledgments

Appendix A. Quasi-square vs rectangular fluid grid

The spectral displacement of the beam $r_a = 16$ using two different sets of fluid grids is calculated. The first is called the rectangular grid, where $\mathcal{N}_y = (\mathcal{N}_x - 1)/r$. The second type is named the quasi-square grid, for which $\mathcal{N}_y = (\mathcal{N}_x - 1)$. Fig. 30a and b show the absolute displacement spectrum $|\hat{\phi}_c|$ of the free corner of the beam with the rectangular and quasi-square grids, respectively.

The displacement ϕ_c varies significantly with the rectangular grid depending on the total number of points. This is clearly seen in the close-up view in Fig. 30a. The resonance frequency increases from the fluid grid 33 x 2 to the grid 64 x 4, and for finer grids, the resonance frequency decreases, and ϕ_c approaches Sader's solution. Although not yet converging to Sader's solution even with a grid of 513 x 32 (total of 16416 points). With the quasi-square grid, on the other hand, a ϕ_c that quickly converges to Sader's solution with the 129 x 128 fluid grid (total of 16512 points) is obtained. The reason a finer discretization fluid grid is required in y-direction lies in the variation of the pressure jump (see Fig. 17), which is high in the y-axis due to the inverse square-root singularity towards the edges. In the x-axis, the variation of the pressure jump is linearly dependent on the variation of the plate's displacement, which results in smaller pressure gradient in x-direction, and thus requiring coarser discretization. In the present paper's analy-
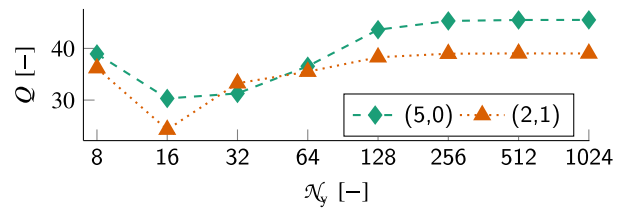
Fig. 31. Quality factors of the (5,0) and (2,1) modes of the slender beam with $r_a = 8$ in water obtained with different quasi-square fluid grids.
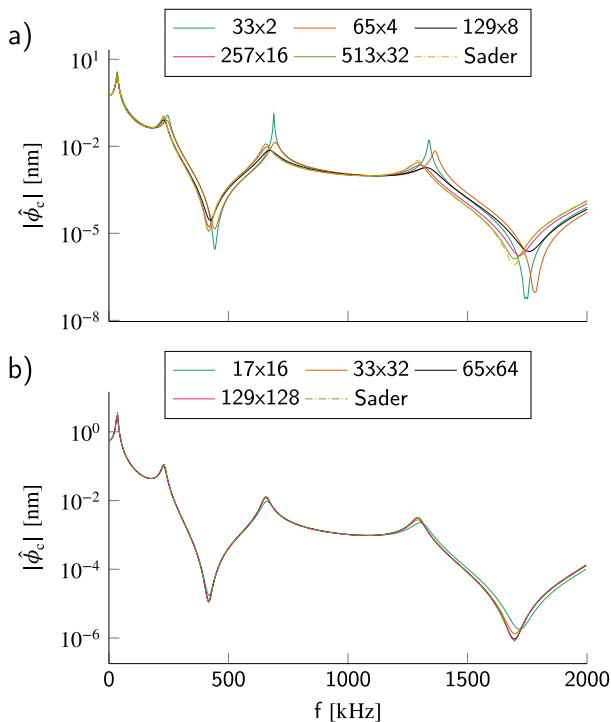
Fig. 30. Absolute displacement spectrum $|\hat{\phi}_c|$ of the beam with $r_a = 16$ with a) a quasi-square fluid grid $\mathcal{N}_y = (\mathcal{N}_x - 1)/r_a$, and b) a rectangular fluid grid $\mathcal{N}_y = (\mathcal{N}_x - 1)$.
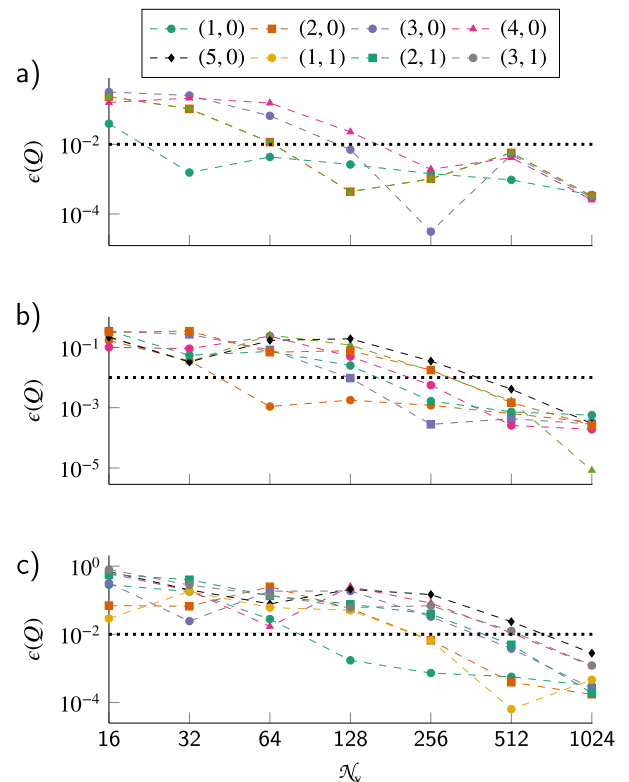
Fig. 32. Convergence of quality factor $\epsilon(Q^i)$ for the flexural modes $(n_x, 0)$ and torsional modes $(n_x, 1)$ of the slender plates with a) $r_a = 16$, b) $r_a = 8$ and c) $r_a = 4$. The dotted black line stands for $\epsilon(Q) = 0.01$, value at which the Q-factor for this mode is considered converged.

ses, the quasi-square fluid grid independent of the plate's aspect ratio is employed, since the quasi-square fluid grid provides faster convergence.

Appendix B. Convergence of Q-factor and resonance frequency

The Q-factors of all the vibrational modes alter with the number of points in the fluid grid. As an example, Fig. 31 shows the Q-factor of the (5,0) and (2,1) modes of the slender beam with $r_a = 8$ in water. As the number of points in y-direction $\mathcal{N}_y$ increases, Q converges to a stable value with a fine enough fluid grid.

The convergence of the quality factor is quantified according to

$$\epsilon\left(Q^i\right) = \frac{|Q^i - Q^{i-1}|}{\max\left(Q_n^i, Q_n^{i-1}\right)}, \tag{B.1}$$

where Q^i and Q^{i-1} are quality factors obtained with two consecutively refined fluid grids for a same vibrating mode. Fig. 32 shows $\epsilon\left(Q^i\right)$ for all modes of the plates with aspect ratio $r_a = 16, r_a = 8$ and $r_a = 4$.

The Q-factor of lower order modes converge with a coarser fluid grid than the Q-factor of higher order modes. For instance, the (1,0) mode of the slender plate with $r_a = 16$ converges for $\mathcal{N}_y \geq 32$. The mode (4,0) of the same plate requires $\mathcal{N}_y \geq 256$ for Q-factor convergence. Furthermore, the wider the plate, the finer the fluid grid required for a converged quality factor. The Q-factor of the mode (4,0) of the plate with $r_a = 4$ requires a discretization with $\mathcal{N}_y \geq 512$ for convergence. The Q-factors of all modes of the slender structures converge with $\epsilon(Q) \leq 0.01$ with a fluid grid of at least 1025 x 1024 points.
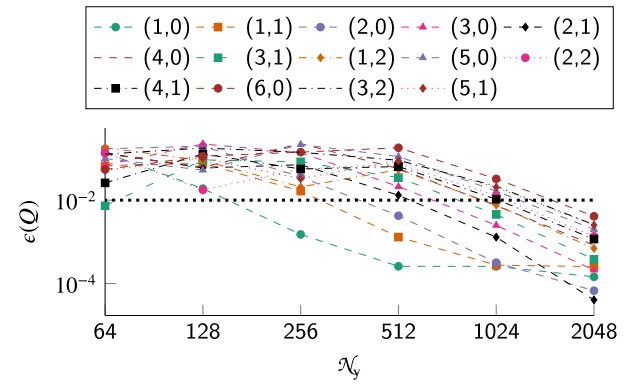

Fig. B.34. Convergence of quality factor for all the vibrational modes of the plate with $r_a = 2$.
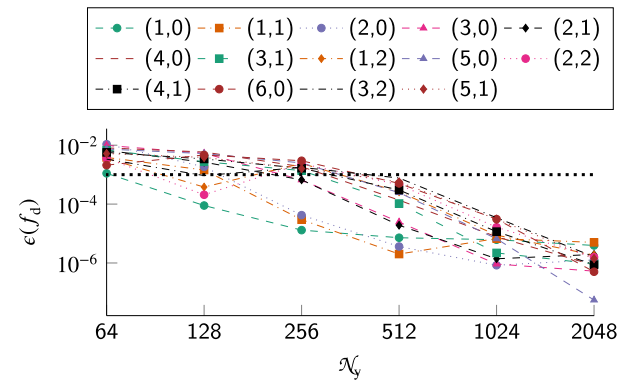

Fig. B.35. Convergence of the resonance frequencies of the plate with $r_a = 2$.

Similarly to the quality factor convergence, the convergence of the resonance frequency is determined with

$$\epsilon(f_d) = \frac{|f_d^i - f_d^{i-1}|}{\max\left(f_d^i, f_d^{i-1}\right)}, \tag{B.2}$$

where f_d^i and f_d^{i-1} are resonance frequencies obtained with two consecutively refined fluid grids for a same vibrating mode. Fig. B.33 shows the convergence of the resonance frequency of the slender plates. Convergence is achieved when $\epsilon(f_d) \leq 0.001$. f_d varies less with the fluid grid than the Q-factor. For this reason, $\epsilon(f_d) \leq 0.001$ is fulfilled with coarser fluid grids than required for the Q-factor convergence.

Convergences of the Q-factor and of the resonance frequencies of the rectangular plate are shown in Figs. B.34 and B.35, respectively. Both convergence criteria ($\epsilon(Q) \leq 0.01$ and $\epsilon(f_d) \leq 0.001$) are met for all vibrational modes with a fluid grid of 2049 x 2048 points.

Fig. B.36 shows the convergence of the Q-factor of the roof tile-shaped modes of the square plate. All roof tile-shaped modes converge with $\epsilon(Q) \leq 0.01$ with a fluid grid of 8193×8192 points.

Fig. B.33. Convergence of the resonance frequencies f_d of the slender plates with a) $r_a = 16$, b) $r_a = 8$ and c) $r_a = 4$. The dotted black line stands for $\epsilon(f_d) = 0.001$, value at which convergence of f_d is achieved.

References

[1] Ahsan SN, Aureli M. Small amplitude oscillations of a shape-morphing plate immersed in a viscous fluid near a solid wall. J Appl Phys 2018;124. https://doi.org/10.1063/1.5046545.

[2] Ahsan SN, Aureli M. Three-dimensional analysis of hydrodynamic forces and power dissipation in shape-morphing cantilevers oscillating in viscous fluids.
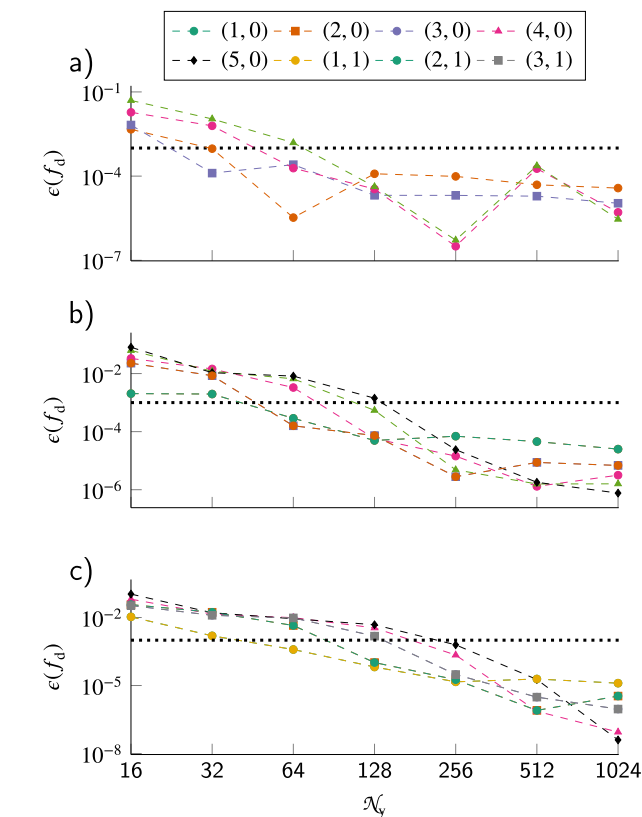
Int J Mech Sci 2018;149:436–51. https://doi.org/10.1016/j.ijmecsci.2017.09.034.

[3] Ahsan SN, Aureli M. Torsional oscillations of a shape-morphing plate in viscous fluids. In: ASME 2019 Dynamic Systems and Control Conference, DSCC 2019 2. https://doi.org/10.1115/DSCC2019-9187.

[4] Arnold D, Brezzi F, Cockburn B, Marini LD. Unified analysis of Discontinuous Galerkin Method for elliptic problems. SIAM J Numer Anal 2002;39:1749–79. https://doi.org/10.1137/S0036142901384162.

[5] Basak S, Raman A, Garimella SV. Hydrodynamic loading of microcantilevers vibrating in viscous fluids. J Appl Phys 2006;99. https://doi.org/10.1063/1.2202232.

[6] Bassi F, Rebay S. A High-Order Accurate Discontinuous Finite Element Method for the Numerical Solution of the Compressible Navier-Stokes Equations. J Comput Phys 1997;131:267–79. https://doi.org/10.1006/jcph.1996.5572.

[7] Bidkar RA, Kimber M, Raman A, Bajaj AK, Garimella SV. Nonlinear aerodynamic damping of sharp-edged flexible beams oscillating at low KeuleganCarpenter numbers. J Fluid Mech 2009;634:269–89. https://doi.org/10.1017/S0022112009007228.

[8] Brand, O., Dufour, I., Heinrich, S.M., Josse, F. (Eds.), 2015. Resonant MEMS: fundamentals, implementation, and application. Wiley-VCH.

[9] Brezzi F, Manzini G, Marini D, Pietra P, Russo A. Discontinuous Galerkin approximations for elliptic problems. Numer Methods Partial Differential Eq 2000;16:365–78. https://doi.org/10.1002/1098-2426(200007)16:4<365::AID-NUM2>3.0.CO;2-Y.

[10] Brumley DR, Willcox M, Sader JE. Oscillation of cylinders of rectangular cross section immersed in fluid. Phys Fluids 2010;22:1–15. https://doi.org/10.1063/1.3397926.

[11] Castille C, Dufour I, Lucat C. Longitudinal vibration mode of piezoelectric thick-film cantilever-based sensors in liquid media. Appl Phys Lett 2010;96:18–21. https://doi.org/10.1063/1.3387753.

[12] Cellini F, Intartaglia C, Soria L, Porfiri M. Effect of hydrodynamic interaction on energy harvesting in arrays of ionic polymer metal composites vibrating in a viscous fluid. Smart Mater Struct 2014;23. https://doi.org/10.1088/0964-1726/23/4/045015.

[13] Cen S, Shang Y. Developments of mindlin-reissner plate elements. Math Probl Eng 2015;2015. https://doi.org/10.1155/2015/456740.

[14] Chen Z, Shatara S, Tan X. Modeling of biomimetic robotic fish propelled by an ionic polymermetal composite caudal fin. IEEE/ASME Trans Mechatron 2010;15:448–59. https://doi.org/10.1109/TMECH.2009.2027812.

[15] Chon JW, Mulvaney P, Sader JE. Experimental validation of theoretical models for the frequency response of atomic force microscope cantilever beams immersed in fluids. J Appl Phys 2000;87:3978–88. https://doi.org/10.1063/1.372455.

[16] Clark MT, Paul MR. The stochastic dynamics of an array of atomic force microscopes in a viscous fluid. Int J Non-Linear Mech 2007;42:690–6. https://doi.org/10.1016/j.ijnonlinmec.2006.10.003.

[17] Clarke RJ, Bachtiar V, Lee TC, Cater JE, Minton J. Response of a fluid-immersed microcantilever close to a deformable body. J Appl Phys 2015;117. https://doi.org/10.1063/1.4913602.

[18] Clarke RJ, Jensen OE, Billingham J. Three-dimensional elastohydrodynamics of a thin plate oscillating above a wall. Phys Rev E - Stat, Nonlinear, Soft Matter Phys 2008;78:1–17. https://doi.org/10.1103/PhysRevE.78.056310.

[19] Cox R, Josse F, Heinrich SM, Brand O, Dufour I. Characteristics of laterally vibrating resonant microcantilevers in viscous liquid media. J Appl Phys 2012;111. https://doi.org/10.1063/1.3674278.

[20] Dung NT, Wells GN. A study of discontinuous Galerkin methods for thin bending problems. III Eur Conf Comput Mech 2008:653. https://doi.org/10.1007/1-4020-5370-3_653.

[21] Embar A, Dolbow J, Harari I. Imposing Dirichlet boundary conditions with Nitsche's method and spline-based finite elements. Int J Numer Meth Eng 2010;83:877–98. https://doi.org/10.1002/nme.2863.

[22] Engel G, Garikipati K, Hughes TJ, Larson MG, Mazzei L, Taylor RL. Continuous/discontinuous finite element approximations of fourth-order elliptic problems in structural and continuum mechanics with applications to thin beams and plates, and strain gradient elasticity. Comput Methods Appl Mech Eng 2002;191:3669–750. https://doi.org/10.1016/S0045-7825(02)00286-4.

[23] Erturk A, Delporte G. Underwater thrust and power generation using flexible piezoelectric composites: An experimental investigation toward self-powered swimmer-sensor platforms. Smart Mater Struct 2011;20. https://doi.org/10.1088/0964-1726/20/12/125013.

[24] Facci AL, Porfiri M. Analysis of three-dimensional effects in oscillating cantilevers immersed in viscous fluids. J Fluids Struct 2013;38:205–22. https://doi.org/10.1016/j.jfluidstructs.2012.11.006.

[25] Fantner GE, Barbero RJ, Gray DS, Belcher AM. Kinetics of antimicrobial peptide activity measured on individual bacterial cells using high-speed atomic force microscopy. Nat Nanotechnol 2010;5:280–5. https://doi.org/10.1038/nnano.2010.29.

[26] Fernández-Méndez S, Huerta A. Imposing essential boundary conditions in mesh-free methods. Comput Methods Appl Mech Eng 2004;193:1257–75. https://doi.org/10.1016/j.cma.2003.12.019.

[27] Frangi A, Bugada A, Martello M, Savadkoohi P. Validation of pml-based models for the evaluation of anchor dissipation in mems resonators. Eur J Mech-A/Solids 2013;37:256–65. https://doi.org/10.1016/j.euromechsol.2012.06.008.

[28] Ghatkesar MK, Braun T, Barwich V, Ramseyer JP, Gerber C, Hegner M, Lang HP. Resonating modes of vibrating microcantilevers in liquid. Appl Phys Lett 2008;92:10–3. https://doi.org/10.1063/1.2838295.

[29] Giessibl FJ. Advances in atomic force microscopy. Rev Mod Phys 2003;75:949–83. https://doi.org/10.1103/RevModPhys.75.949.

[30] Graham MD. Microhydrodynamics, Brownian motion, and complex fluids, volume 58. Cambridge University Press; 2018.

[31] Green CP, Sader JE. Torsional frequency response of cantilever beams immersed in viscous fluids with applications to the atomic force microscope. J Appl Phys 2002;92:6262–74. https://doi.org/10.1063/1.1512318.

[32] Green CP, Sader JE. Small amplitude oscillations of a thin beam immersed in a viscous fluid near a solid surface. Phys Fluids 2005;17:1–12. https://doi.org/10.1063/1.1995467.

[33] Holzl W, Behlert R, Gehring M, Schrag G. Enhanced fluid flow by wavelike excitation of a micromechanical bending actuator. In: 2019 20th International Conference on Thermal, Mechanical and Multi-Physics Simulation and Experiments in Microelectronics and Microsystems, EuroSimE 2019. https://doi.org/10.1109/EuroSimE.2019.8724585.

[34] Hopcroft MA, Nix WD, Kenny TW. What is the young's modulus of silicon? J Microelectromech Syst 2010;19:229–38. https://doi.org/10.1109/JMEMS.2009.2039697.

[35] Hosaka H, Itao K, Kuroda S. Damping characteristics of beam-shaped micro-oscillators. Sens Actuat A: Phys 1995;49:87–95. https://doi.org/10.1016/0924-4247(95)01003-J.

[36] Intartaglia C, Soria L, Porfiri M. Hydrodynamic coupling of two sharp-edged beams vibrating in a viscous fluid. In: Proceedings of the Royal Society A: Mathematical, Physical and Engineering Sciences 470. https://doi.org/10.1098/rspa.2013.0397.

[37] Karniadakis G, Beskok A, Aluru N. Microflows and nanoflows: fundamentals and simulation, volume 29. Springer Science & Business Media; 2006.

[38] Kirby BJ. Micro-and nanoscale fluid mechanics: transport in microfluidic devices. Cambridge University Press; 2010.

[39] Kucera M, Wistrela E, Pfusterschmied G, Ruiz-Díez V, Sánchez-Rojas JL, Schalko J, Bittner A, Schmid U. Characterisation of multi roof tile-shaped out-of-plane vibrational modes in aluminium-nitride-actuated self-sensing micro-resonators in liquid media. Appl Phys Lett 2015;107:1–5. https://doi.org/10.1063/1.4928429.

[40] Larsson K, Larson MG. Continuous piecewise linear finite elements for the Kirchhoff-Love plate equation. Numer Math 2012;121:65–97. https://doi.org/10.1007/s00211-011-0429-5.

[41] Leissa AW. The Free vibration of rectangular plates. J Sound Vib 1973;31:257–93. https://doi.org/10.4324/9780203015711.

[42] Liem AT, Ari AB, Ti C, Cops MJ, McDaniel JG, Ekinci KL. Nanoflows induced by mems and nems: Limits of two-dimensional models. Phys Rev Fluids 2021;6:024201. https://doi.org/10.1103/PhysRevFluids.6.024201.

[43] Logg A, Mardak LA, Wells GN. Automated solution of differential equations by the finite element method: The FEniCS book. 84 ed.,. Springer Science & Business Media; 2012.

[44] Maali A, Hurth C, Boisgard R, Jai C, Cohen-Bouhacina T, Aim JP. Hydrodynamics of oscillating atomic force microscopy cantilevers in viscous fluids. J Appl Phys 2005;97. https://doi.org/10.1063/1.1873060.

[45] Olgaard KB, Logg A, Wells GN. Automated code generation for discontinuous galerkin methods. Soc Industr Appl Math 2007;31:849–64. https://doi.org/10.1137/090750688.

[46] Patocka F, Schlögl M, Schneidhofer C, Dörr N, Schneider M, Schmid U. Piezoelectrically excited MEMS sensor with integrated planar coil for the detection of ferrous particles in liquids. Sens Actuat, B: Chem 2019;299:126957. https://doi.org/10.1016/j.snb.2019.126957.

[47] Pfusterschmied G, Toledo J, Kucera M, Steindl W, Zemann S, Ruiz-Díez V, Schneider M, Bittner A, Sanchez-Rojas JL, Schmid U. Potential of piezoelectric MEMS resonators for grape must fermentation monitoring. Micromachines 2017;8. https://doi.org/10.3390/mi8070200.

[48] Pfusterschmied G, Weinmann C, Schneider M, Platz D, Shen N, Sader J, Schmid U. Sound dissipation from plate-type resonators excited in non-conventional transversal modes in liquids. J Micromech Microeng 2020;30. https://doi.org/10.1088/1361-6439/ab8bc9.

[49] Platz D, Schmid U. Vibrational Modes in MEMS Resonators. J Micromech Microeng 2019;29:123001. https://doi.org/10.1088/1361-6439/ab4bad.

[50] Pozrikidis C. A singularity method for unsteady linearized flow. Phys Fluids A 1989;1:1508–20. https://doi.org/10.1063/1.857329.

[51] Pozrikidis C. Boundary integral and singularity methods for linearized viscous flow. Cambridge University Press; 1992.

[52] Raman A, Melcher J, Tung R. Cantilever dynamics in atomic force microscopy. Nano Today 2008;3:20–7. https://doi.org/10.1016/S1748-0132(08)70012-4.

[53] Reddy JN. Theory and Analysis of Elastic Plates and Shells. Taylor & Francis; 2007.

[54] Ricci A, Canavese G, Ferrante I, Marasso SL, Ricciardi C. A finite element model for the frequency spectrum estimation of a resonating microplate in a microfluidic chamber. Microfluid Nanofluid 2013;15:275–84. https://doi.org/10.1007/s10404-013-1146-4.

[55] Ruiz-Díez V, Hernando-García J, Manzaneque T, Kucera M, Schmid U, Sánchez-Rojas JL. Modelling out-of-plane and in-plane resonant modes of microplates in liquid media. J Micromech Microeng 2015;25. https://doi.org/10.1088/0960-1317/25/7/074005.

[56] Ruiz-Díez V, Hernando-García J, Toledo J, Manzaneque T, Kucera M, Pfusterschmied G, Schmid U, Sánchez-Rojas JL. Modelling and characterization of the roof tile-shaped modes of AlN-based cantilever resonators in liquid media. J Micromech Microeng 2016;26. https://doi.org/10.1088/0960-1317/26/8/084008.

[57] Sader JE. Frequency response of cantilever beams immersed in viscous fluids with applications to the atomic force microscope. J Appl Phys 1998;84:64–76. https://doi.org/10.1063/1.368002.

[58] Schmid S, Jensen K, Nielsen K, Boisen A. Damping mechanisms in high-q micro and nanomechanical string resonators. Phys Rev B 2011;84:165307. https://doi.org/10.1103/PhysRevB.84.165307.

[59] Shrestha B, Ahsan SN, Aureli M. Experimental study of oscillating plates in viscous fluids: Qualitative and quantitative analysis of the flow physics and hydrodynamic forces. Phys Fluids 2018;30. https://doi.org/10.1063/1.5001330.

[60] Takizawa K, Tezduyar TE. Multiscale space-time fluid-structure interaction techniques. Comput Mech 2011;48:247–67. https://doi.org/10.1007/s00466-011-0571-z.

[61] Thomsen EV, Reck K, Skands G, Bertelsen C, Hansen O. Silicon as an anisotropic mechanical material: Deflection of thin crystalline plates. Sens Actuat A: Phys 2014;220:347–64. https://doi.org/10.1016/j.sna.2014.09.007.

[62] Tuck EO. Calculation of unsteady flows due to small motions of cylinders in a viscous fluid. J Eng Math 1969;3:29–44. https://doi.org/10.1007/BF01540828.

[63] Tung RC, Jana A, Raman A. Hydrodynamic loading of microcantilevers oscillating near rigid walls. J Appl Phys 2008;104. https://doi.org/10.1063/1.3033499.

[64] Van Eysden CA, Sader JE. Small amplitude oscillations of a flexible thin blade in a viscous fluid: Exact analytical solution. Phys Fluids 2006;18. https://doi.org/10.1063/1.2395967.

[65] Van Eysden CA, Sader JE. Frequency response of cantilever beams immersed in compressible fluids with applications to the atomic force microscope. J Appl Phys 2009;106. https://doi.org/10.1063/1.3254191.

[66] Voigt P, Schrag G, Wachutka GK. Electrofluidic full-system modelling of a flap valve micropump based on Kirchhoffian network theory. Sens Actuat, A 1998;66:9–14. https://doi.org/10.1016/S0924-4247(97)01783-4.

[67] Wells GN, Dung NT. A C0 discontinuous Galerkin formulation for Kirchhoff plates. Comput Methods Appl Mech Eng 2007;196:3370–80. https://doi.org/10.1016/j.cma.2007.03.008.

[68] Zhang WM, Meng G, Wei X. A review on slip models for gas microflows. Microfluid Nanofluid 2012;13:845–82. https://doi.org/10.1007/s10404-012-1012-9.